

# IMPROVING ON A MODEL FOR ANTIDEUTERON PRODUCTION

by

Thomas Haaland

THESIS  
for the degree of  
MASTER OF SCIENCE



Faculty of Mathematics and Natural Sciences  
University of Oslo

1. February 2018



# Abstract

Antideuterons are a potential source for detecting dark matter. Its annihilation or decay in our galaxy could provide a small glow of antideuterons with very low backgrounds. New detectors for the special purpose of detecting these antimatter particles are being designed and built. To this end the standard coalescence model is being pushed to its limits. Here we will examine a new model, the cross section model, designed to supplement the coalescence model and implement a weighting method in an attempt to increase the accuracy of both the coalescence and cross section models.



To Mari and to my mother.



# Acknowledgements

Many thanks to Are Raklev for his guidance and insight. We are grateful to Lars A. Dal for help with the cross section method and for providing data from the ALICE experiment.

The CPU intensive part of this work was performed on the Abel Cluster, owned by the University of Oslo and the Norwegian metacenter for High Performance Computing (NOTUR), and operated by the Research Computing Services group at USIT, the University of Oslo IT-department. The computing time was given by NOTUR allocation NN9284K, financed through the Research Council of Norway.



# Contents

<b>1</b>	<b>Introduction</b>	<b>1</b>
<b>2</b>	<b>Dark matter</b>	<b>3</b>
2.1	Motivations for dark matter . . . . .	3
2.1.1	Zwicky and the Coma cluster . . . . .	3
2.1.2	Galaxy rotation curves . . . . .	4
2.1.3	Gravitational lensing . . . . .	6
2.1.4	Cosmic microwave background radiation . . . . .	7
2.1.5	Baryon acoustic oscillations . . . . .	9
2.1.6	Structure formation . . . . .	10
2.2	Possible explanations and searches for dark matter . . . . .	10
2.2.1	Possible explanations for dark matter . . . . .	11
2.2.2	Indirect detection . . . . .	12
2.2.3	Collider searches . . . . .	13
2.2.4	Direct detection . . . . .	13
2.3	Dark matter models . . . . .	14
2.3.1	Weakly Interacting Massive Particles . . . . .	14
2.3.2	Supersymmetry and the neutralino . . . . .	14
2.3.3	Gravitino – decaying dark matter . . . . .	16
<b>3</b>	<b>Antideuteron searches</b>	<b>19</b>
3.1	Antideuteron, a search channel with low noise . . . . .	19
3.2	BESS-Polar II . . . . .	19
3.3	AMS-02 . . . . .	20
3.4	GAPS – the General AntiParticle Spectrometer . . . . .	21
<b>4</b>	<b>Antideuteron production models</b>	<b>23</b>
4.1	Coalescence model . . . . .	23
4.2	Cross section model . . . . .	25
4.2.1	Finalstate kinematics . . . . .	28
4.3	Comparing models to experiment . . . . .	31

## Contents

<b>5 Improving antideuteron production models</b>	<b>35</b>
5.1 Comparing measured $p$ and $\bar{p}$ spectra to Monte Carlo models . . . . .	35
5.2 Reweighting . . . . .	38
5.3 Reweighted $\bar{d}$ spectra . . . . .	38
<b>6 Conclusion</b>	<b>45</b>
<b>Bibliography</b>	<b>47</b>

# Chapter 1

## Introduction

Dark matter have eluded discovery for almost a century. Though there are compelling evidence dark matter should exist. In this thesis we will discuss some motivations for dark matter and then some particle candidates. There are reasons to believe these candidates leaves a signature background radiation of antideuterons, which is especially relevant since few other processes produce a signal in this channel. In order to better predict the antideuteron spectrum makes improving Monte Carlo models for antideuteron production important. We will study two Monte Carlo models for antideuteron production and finally introduce a weighting method in an attempt to improve on the models predictions.



# Chapter 2

## Dark matter

In this chapter we will look at some discoveries which motivates dark matter. Then we will explore some possible explanations for what it is and what this means for detecting it. Finally, we will finally look at some models which predicts the existence of dark matter.

### 2.1 Motivations for dark matter

Dark matter has been invoked at several occasions to explain anomalies and was mentioned as early as 1933 by Fritz Zwicky. He noticed that distant galaxies had too much kinetic energy compared to the gravitational potential of the visible stars. This suggested some unseen matter made up the difference. It has also been suggested that our gravitational theories may behave unexpectedly at great distances, but in this thesis I will assume dark matter can be explained as matter and not consider revised gravitational theory.

#### 2.1.1 Zwicky and the Coma cluster

The first hint of dark matter came in 1933 when Fritz Zwicky used the virial theorem on the Coma cluster and found that the cluster ought to weigh around 400 times more than the mass he could infer from constituent stars. He called this excess matter for 'dunkle matter' [1].

The virial theorem states

$$\langle T \rangle = -\frac{1}{2} \sum_{k=1}^N \langle \mathbf{F}_k \cdot \mathbf{r}_k \rangle , \quad (2.1)$$

and relates the time averaged kinetic energy of a system  $\langle T \rangle$  to its time averaged

total potential energy  $\langle V_{tot} \rangle$ :

$$\langle T \rangle = - \sum_k^N m_k \langle v_k^2 \rangle = -\frac{1}{2} \langle V_{tot} \rangle. \quad (2.2)$$

In his article Zwicky used the virial theorem to put a lower bound on the mass  $M$  of the Coma cluster:

$$M > \frac{3R \langle \bar{v}_s^2 \rangle}{5G}. \quad (2.3)$$

Here  $R$  is the radius of a uniformly distributed sphere (simulating the cluster),  $G$  is the universal gravitational constant,  $\langle \bar{v}_s^2 \rangle$  is the velocity double averaged with respect to time and mass, assuming a spherically symmetric distribution of velocity and velocity component as measured from the direction of the observer. Since hydrogen is the dominant element in stars we can use hydrogen absorption lines to determine doppler shift and consequently the stars velocity relative to us.

From measurements the Coma cluster ought to have a mass greater than

$$M > 9 \times 10^{46} \text{g}. \quad (2.4)$$

The Coma cluster contain about one thousand nebulae, yielding the average mass of

$$\bar{M} > 9 \times 10^{43} \text{g} = 4.5 \times 10^{10} M_\odot. \quad (2.5)$$

Zwicky compared an average nebulae with the luminosity of about  $L_{nebula} = 8.5 \times 10^7 L_\odot$  [1] with  $\bar{M}$ , yielding a conversion factor  $\gamma = \frac{\bar{M}}{L_{nebula}} \approx 500 \frac{M_\odot}{L_\odot}$  between luminosity and mass. He then points out that a similar conversion factor for the local Kapteyn stellar system has  $\gamma' = 3 \frac{M_\odot}{L_\odot}$ . The portion of the mass in the Kapteyn system which are luminous are much greater than the average in the Coma cluster. Zwicky subsequently couldn't find this missing luminous mass, which he dubbed 'dunkle matter'.

### 2.1.2 Galaxy rotation curves

Using the doppler effect dark matter can be suspected by looking at galaxy rotation curves. Since hydrogen is the dominant element in stars we can use hydrogen absorption lines to determine doppler shift and consequently the stars velocity relative to the other stars in the galaxy in the direction of the observer. Plotting out the distribution of velocities as a function of distance to the galaxy core gives a galaxy rotation curve.

If we assume classical mechanics hold and the matter we see in terms of stars and is all the matter there is, we would expect the velocities of stellar bodies to

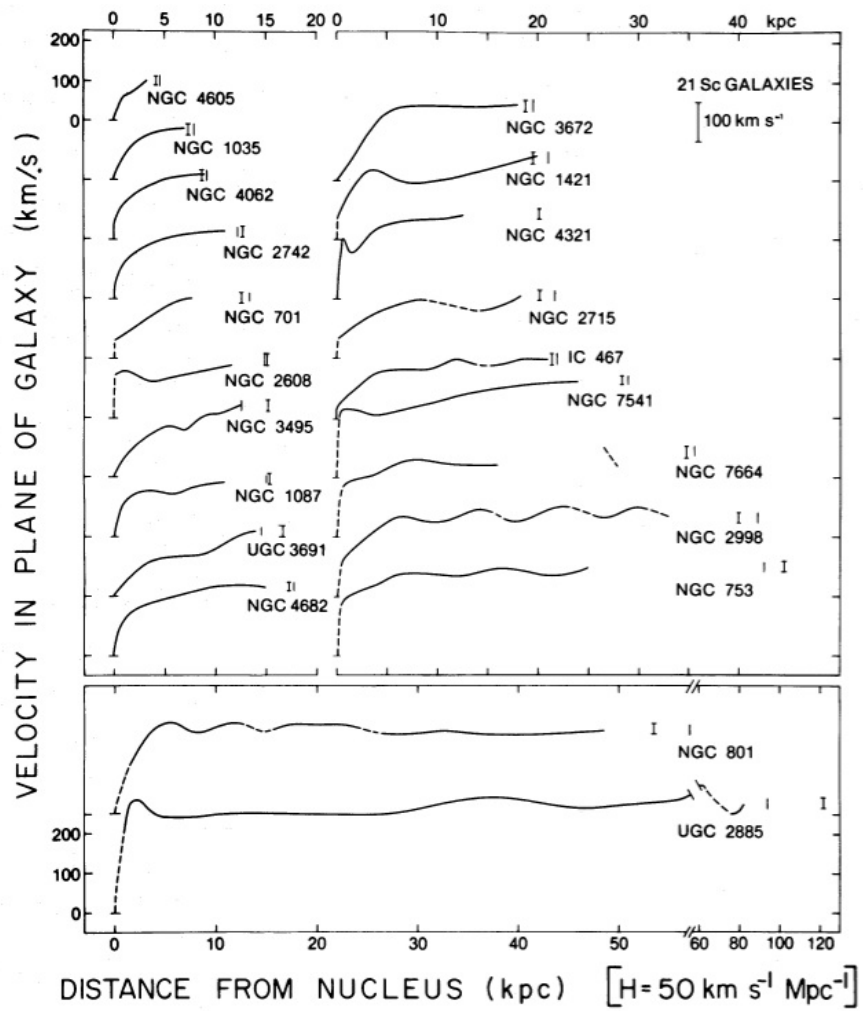


**Figure 2.1:** Some of the galaxy rotation curves investigated by Vera Rubin from her paper [2].



**Figure 2.2:** Gravitational lensing causing distant galaxies appear as circles.

fall off to zero as the distance to the galaxy center increases. The velocities of stellar bodies as a function of distance from the galactic center is called a galaxy rotation curve. From figure 2.1 what we see is that velocity tends to flatten or increase with radius instead. Rubin concludes that the shape of the galaxy rotation curves implies that the mass is not centrally located, but is instead spherically distributed across the galaxy [2]. If the shape of the galaxy rotation curve is due to unseen matter this matter needs to be distributed with close to uniform density near the galaxy core. The density appear to taper to zero some distance outside of the outer bounds of the visible part of the galaxy.

Rubin also note that the galaxy rotation curves appear to sit on a common curve. So that the smaller galaxies have a curve which is part of the rotation curve of a larger galaxy, but just truncated at a smaller radius  $R$ . This further implies most galaxies sits in a similar gravitational potential well predominantly determined by non-luminous matter.

### 2.1.3 Gravitational lensing

General Relativity predicts that light is bent near massive objects such as shown in figure 2.2. The deflection angle is [3]

$$\delta\theta = \frac{4GM(r)}{rc^2}, \quad (2.6)$$

where  $G$  is the gravitational constant and  $M(r)$  is the total mass interior to the projected radius  $r$ .

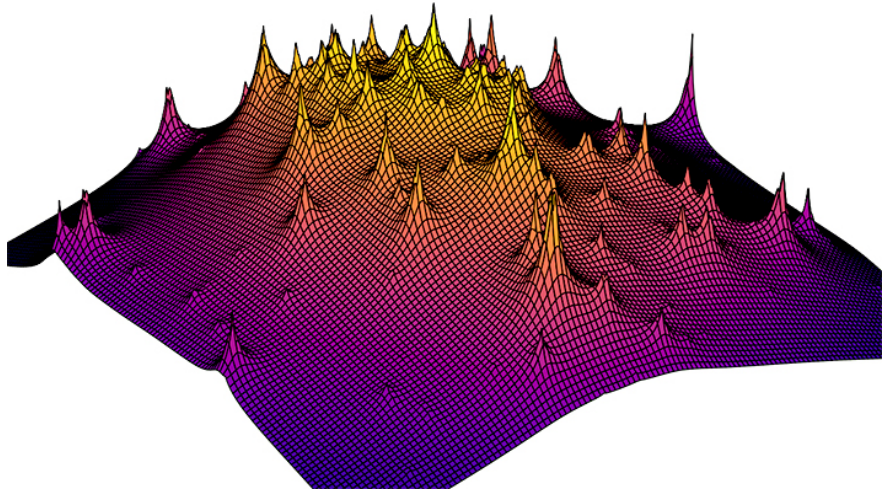


**Figure 2.3:** Map of mass contained in the galaxy cluster MACSJ 0416. The mapping is made using lensing techniques [4].

Using deflection of light due to gravitational lensing Natarajan and others [4] solved for the mass in and around galaxies in galaxy clusters. When applied to a galaxy cluster such as MACSJ 0416 it is found that most of the mass is smoothly distributed between galaxies. From figure 2.3 most of the mass in the galaxy cluster appear to be between galaxies.

Even though most mass in galaxy clusters seem to be between galaxies it is still not clear what this mass is. At least some of this mass should be dust. To determine how much if not all of the mass in galaxy clusters are dust we can study colliding galaxies. It is expected that when galaxies collide the stars should pass by each other and very little friction is expected and should change momentum only according to gravity. Dust, however, is much more smoothly distributed and ought to feel friction and slow down as the galaxies collide. One such colliding cluster of galaxies studied is the Bullet cluster (figure 2.4).

From studying the Bullet cluster it appears most of the matter in a galaxy cluster is neither contained in the galaxies as luminous matter nor distributed as dust. Most mass in the clusters seems to be both smoothly distributed, non-radiating and friction less.

#### 2.1.4 Cosmic microwave background radiation

Inflation theory predicts a smooth early universe consistent with measurements. To see this we can study the metric in the standard  $\Lambda$ CDM (Lambda cold dark matter) model. This model is a parametrization of the Big Bang cosmological model which also have a cosmological constant  $\Lambda$ . The cosmological constant is associated with dark energy and is responsible for the expanding universe. The



**Figure 2.4:** The Bullet cluster. By using gravitational lensing most of the mass is determined to be located in the blue area. Dust is determined by radiative methods to be located mostly in the red area.

metric which describes an inflating universe is

$$ds^2 = -(1 - \Lambda r^2)dt^2 + \frac{1}{1 - \Lambda r^2}dr^2 + r^2 d\Omega^2. \quad (2.7)$$

Here  $ds^2$  is the line element in a universe with a non zero-cosmological constant  $\Lambda$  in spherical coordinates. This metric is similar to an inverted Schwarzschild metric and there is a horizon at  $r^2 = 1/\Lambda$  called the cosmological horizon. Some observer at  $r \neq 0$  will drift in an accelerating manner away from  $r = 0$ . Also, in the same way that any irregularities in space gets smoothed out close to the event horizon around a black hole, irregularities approaching the cosmological horizon are smoothed. From this we expect the early universe after inflation to be uniform and smooth.

Still, the universe should not be perfectly smooth due to quantum fluctuations. This variation leads to some regions being more dense and feeling greater gravitational pull, causing a collapse and leading to overdense regions. While photons and baryonic matter will experience pressure as the region heats, dark matter will not feel the same pressure and will continue to collapse. This leads to a more granular universe, where the granularity can be predicted as dependent on the total dark matter content of the universe [5].

As the early universe expanded the temperature fell. Initially, the temperature was high enough to prevent electrons to settle around the nucleus of atoms

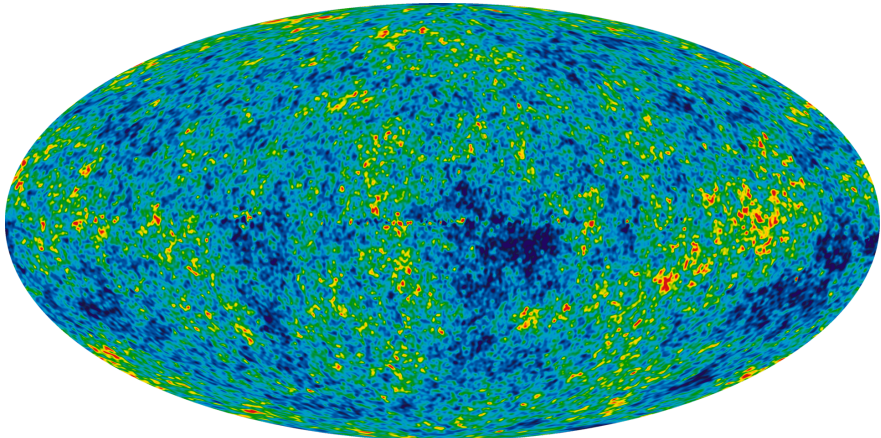


**Figure 2.5:** Temperature variation in the Cosmic Background Radiation measured by WMAP [5]. This image shows the early universe was smooth, but still somewhat granular.

resulting in a plasma soup which was opaque to light. However, as the universe expands temperature dropped sufficient to form hydrogen molecules. Light was now free to travel across the universe. This coagulation moment is now seen as the cosmic background radiation (CMB). When studying the CMB we can see the distribution of matter at the moment of coagulation. As noted above the coarseness of the CMB can be associated with a certain amount of dark matter.

NASA launched the Wilkinson Microwave Anisotropy Probe (WMAP) to map the sky in the frequency range 23 to 94 GHz, while ESA used the Planck radio telescope to map the cosmic microwave background radiation in the frequency range 27 GHz and 1 THz. Their data were used to determine temperature variations in the cosmic background radiation to  $2.72548 \pm 0.00057$  K, as seen in figure 2.5, by WMAP. It was found that the CMB fluctuations observed require dark matter for it to be explained [5].

### 2.1.5 Baryon acoustic oscillations

Before the recombination event, if there were areas of overdensity this area would experience collapse from gravitational forces as well as expansion due to radiation pressure. These counteracting forces caused waves in the plasma analogues to sound in air. The dark matter only experience gravitational pull and so remains in the center of the sound wave. Before the recombination event photons and baryonic matter moved out from the sound wave center. After the recombination event the photons were free to move away from the baryons. This relieved pressure and left the baryonic matter as a shell around a dark matter core. The size of this shell is referred to the sound horizon. At the sound horizon there would be a higher concentration of baryonic matter and more galaxies ought to

be formed here, so most galaxies ought to be separated from each other by the sound horizon distance.

The amount of dark matter in the universe leads to different sound horizon distances and thus provides a way to extrapolate the total amount of dark matter in the universe.

### 2.1.6 Structure formation

As mentioned earlier, dark matter feel an unopposed gravitation pull and because of this would collapse into structures due to gravitational pull earlier than Standard Model matter. Since the universe is slightly perturbed after the inflation phase the dark matter is free to collapse into the areas of higher densities forming dark matter halos early in the history of the universe. These dark matter halos allow galaxies and stars to form much earlier than without dark matter since after the recombination event baryonic matter no longer feel as much radiation pressure and would collapse into overdensities of dark matter already formed.

These perturbations of higher density grows over time, while space itself keeps growing. Simulations indicate the dark matter contribute to form filaments running between hubs of dense matter where galaxy clusters and super clusters form. The size of the hubs and how quickly the universe forms such filaments indicates the amount and the type of dark matter. Hotter dark matter only forms larger structures, while colder dark matter is necessary for forming small structures.

## 2.2 Possible explanations and searches for dark matter

In the previous chapter the existence of dark matter was motivated. In this chapter I will discuss some possible explanations for dark matter and some promising searches given the theories outlined here. As discussed earlier, we can first establish whether it is ordinary (baryonic) matter or if we need to look for particles beyond the Standard Model of physics. If dark matter stems from exotic particles it ought to be possible to detect them directly, indirectly and by means of a particle accelerator. Direct detection relies on dark matter particles interacting directly with a Standard Model particle bouncing off of and producing a kinematic response in the SM particle  $\chi f \rightarrow \chi f$  where  $f$  is a some fermion or antifermion and  $\chi$  is some supersymmetric particle. Indirectly as dark matter particles decay  $\chi \rightarrow f f f$  or annihilate  $\chi \chi \rightarrow f f$  where we observe the resulting fermions. Finally they can be produced in a particle accelerator by combining Standard Model particles  $f f \rightarrow \chi \chi$  where we look for a lack of momentum and energy conservation in the detector.

### 2.2.1 Possible explanations for dark matter

To exclude dust (which we assume to consist mostly of hydrogen) as a primary contributor to dark matter, we can use gravitational lensing on colliding galaxy clusters, such as the Bullet Cluster which were discussed in chapter 2.1.3, to determine the proportion of the galaxy clusters mass which is due to dust. When two galaxy clusters collide, its different constituents behave differently. Stars, planets and other small and dense objects have a very small chance of colliding with each other and will only feel gravitational pull but very little friction and will therefore survive the event without loosing much momentum. Gas, however, would show behaviour closer to that of a liquid and would experience friction. Dark matter is theorized to not feel the electromagnetic force and would not feel friction like dust do.

By using gravitational lensing we are able to see where most of the mass is located, and thus detect whether gas comprise most of the mass between stars. From the Bullet cluster we see that most of the mass is not found in the dust, but remain between the stars of each galaxy. From this we can rule out dust as dark matter.

Massive astrophysical compact halo objects, or MACHOs (brown dwarves, neutron stars, black holes and rogue planets) could be a source of dark matter. Since they do not produce much radiation themselves, they could constitute the missing matter of galaxies. By using microlensing<sup>1</sup> it is found that there are nowhere near enough MACHO's to account for the missing mass in observed galaxies.

While most dark matter cannot be baryonic in nature, the neutrino is a Standard Model candidate. The neutrino is a neutral particle which only feels the weak nuclear force, and would therefore be dark. It also has some mass, although small. We know neutrinos are produced in stars, and plenty of neutrinos ought to have been produced in the early stages of the Universe. However, the neutrinos are so light they invariably have relativistic velocities. This sort of dark matter is referred to as hot dark matter (HDM) and exhibit some behaviour distinct from cold dark matter (CDM). CDM are theorised to be particles with a large mass preventing them from being produced with relativistic velocities. Due to the HDM's higher velocities they would have an easier time escape the gravitational pull of galaxies and contribute to a DM cloud which is more dispersed than a CDM cloud. When we investigate the DM clouds, we find it is not dispersed enough to account for only HDM, there must also be CDM, especially around galaxies. The structure formation from section 2.1.6 indicates that there must be a high contribution from CDM for filaments to form in the manner observed.

Finally, if dark matter was produced in equilibrium with SM particles in the

---

<sup>1</sup>When some MACHO pass in front of some luminous object, they bend the light acting as a lens and increase the luminosity of the luminous object.

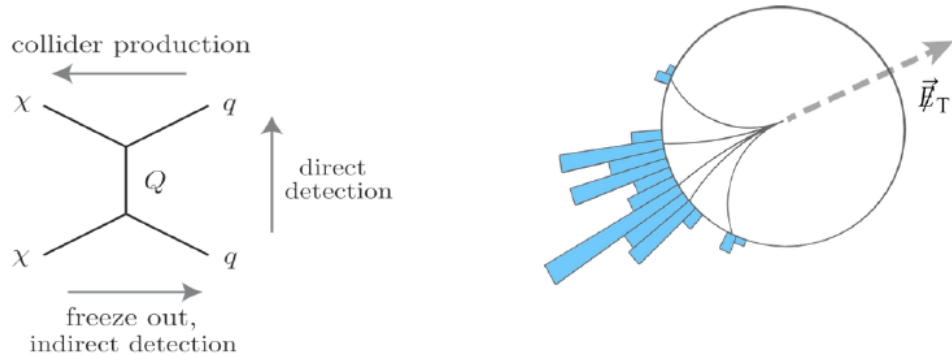


**Figure 2.6:** Left: a schematic representation of the search for dark matter. Right: In collider production CERN look for missing energies and missing momentum (Image taken from [6]).

early universe but 'froze out' as the universe cooled, the dark matter particles ought to have a non zero probability to interact with Standard Model particles. Candidate for such weakly interacting massive particle are called WIMPs. These are hypothesised particles which feel the weak nuclear force and gravity, but not much else. Some such candidates are provided in Supersymmetry, which we discuss in more detail in 2.3.2. Denoted by  $\chi$ , the WIMP ought to be detectable directly, indirectly or in collider production.

### 2.2.2 Indirect detection

Indirect detection focuses on the search for dark matter decay or annihilation products. There are in particular two different candidates I will discuss here. Sterile neutrinos are a hypothetical particle which may be a possible candidate for a cold dark matter particle. Depending on their production mechanism they can provide either hot or cold dark matter. Their possible mass range from 1 keV to tens of keV [7]. If unstable they can be found with X-ray detection via the radiative decay channel  $N \rightarrow \nu\gamma$ .

Supersymmetry predicts some neutral candidates in the given mass range. Of particular interest are the lightest possible supersymmetric particles such as the gravitino and neutralino. They can decay producing a gamma ray  $\chi \rightarrow \gamma X$ , from bremsstrahlung or annihilation  $\chi\chi \rightarrow \gamma X$ .

For the rare  $\chi\chi \rightarrow \gamma\gamma$  the gamma rays are produced back to back with energies related to the dark matter particle mass, which together with a comoving dark matter halo, makes gamma rays well suited for uncovering precise information about the dark matter halo if at all detectable. Also, since the photon does not carry charge, it is not deflected in magnetic fields. So it is easy to trace it back to their source and can be used to search for dark matter signatures

in galaxies other than our own as well as target areas with expected high DM density, such as the galactic centre. Their energy are also limited by the decaying dark matter particle rest mass and provides a unique spectral signature. Finally, in the local universe they don't suffer from attenuation and retain the source spectral information intact at the Earth. Still, the signal strength are expected to be a fraction of the background signal strength [8].

Dark matter are also expected to produce quarks and antiquarks. Protons and neutrons as well as their antimatter partners are expected to be produced in this manner. However, since the rate of decay and annihilation is very low the signal tend to drown in the background astrophysical production. The antimatter particles are of particular interest since there are fewer cosmological processes which leads to antimatter, though antiprotons are still abundant because of pair-production. Production of antideuterons, however, are prime candidates since the noise from normal astrophysical processes is low. Because of this I will single out antideuteron production as particularly important.

### 2.2.3 Collider searches

Collider search, such as done in the LHC, attempts to create dark matter from bottom up. However, to do so requires that the accelerator has more energy than the mass  $2M_\chi$  of the dark matter particle. Since the dark matter particle is expected to have a very small cross section when interacting with any SM particle it is expected to pass right through the detector. At CERN they are therefore looking for missing energy other than what is lost by neutrinos 2.6. No evidence of such a particle have been found, which either suggest an increasingly smaller cross section for any available processes or a mass for the dark matter particle too large to be produced at the LHC.

### 2.2.4 Direct detection

Direct searches try and detect dark matter particles scattering directly off of nuclei. Direct searches suffer from low signal to noise problems which makes analyses difficult particularly at low WIMP mass. With a mass in the GeV-TeV range, we can expect an energy transfer of around 100 keV per event with  $10^{-3}$  events per kg detector material and year [9]. There are many currently running direct search experiments, for instance the LUX and CDMS experiments [10]. To detect these rare and small energy deposits the LUX (Liquid Underground Xenon) dark matter project consists of 370 kg liquid xenon placed 1 mile underground, the large detector size is to compensate for low interaction cross section and placed deep underground to reduce background noise.

## 2.3 Dark matter models

### 2.3.1 Weakly Interacting Massive Particles

If dark matter was in thermal equilibrium with SM particles in the early universe but later froze out due to an expanding and cooling universe, it is assumed dark matter can still interact with normal matter. Indirect searches rely on the kinematic differences between cosmic rays produced in DM decay and normal astrophysical processes which involve SM matter [10]. Studies of dark matter halos around galaxies suggest the dark matter is made from weakly interacting massive particles (WIMPS) and suggests particles with non-relativistic velocities.

The freeze out ought to have left a relic density of dark matter particles. The amount left behind is controlled by their annihilation rate into Standard Model particles since after the freeze out there is no longer enough thermal energy to produce them in collisions and a larger annihilation cross section leads to fewer surviving until decreasing density rules out continuous annihilation. Therefore the dark matter densities today are closely tied to the annihilation cross section of the dark matter particles. The relic density depends only on the annihilation cross section  $\sigma_{ann}$  weighted by the average velocity of the particle [8]

$$\Omega_\chi h^2 = 0.11 \frac{3 \times 10^{-26} \text{cm}^3 \text{s}^{-1}}{\langle \sigma_{ann} v \rangle}. \quad (2.8)$$

From CMB observations the density value of the relic dark matter is  $\Omega_\chi = 0.113 \text{pm}^3 \pm 0.004$ , which means that the velocity-weighted annihilation cross section in the range of  $3 \times 10^{-26} \text{cm}^3 \text{s}^{-1}$ . This gives a cross section of approximately 1pb, which is in the range of the Standard Model weak interaction for  $m_\chi = 10 \text{ GeV}$  [8]. Supersymmetry readily predicts such a particle, and this is referred to as the WIMP miracle. The predicted particles, such as the neutralino, should make up a cloud of non-interacting matter in the universe. They still may annihilate, albeit rarely, and thus give off a glow. Their annihilation is expected to lead to an amount of antideuterons. I will discuss this process in more detail in the next chapter.

### 2.3.2 Supersymmetry and the neutralino

Supersymmetry introduces a symmetry between bosonic and fermionic states, allowing a transformation between the two [11]. The operator  $Q$  is the generator for the transformation such that

$$Q |Boson\rangle = |Fermion\rangle \quad (2.9)$$

and

$$Q |Fermion\rangle = |Boson\rangle. \quad (2.10)$$

This transformation introduces new particles for each Standard Model particle. States  $|\Omega\rangle$  which transform proportionally to some combination of  $Q$  and  $Q^\dagger$  (the hermitian conjugate of  $Q$ ) acting on some other state  $|\Omega'\rangle$  are part of the same supermultiplet, where the supermultiplet, in this case  $|\Omega\rangle$  and  $|\Omega'\rangle$ , is a fermion boson pair.

The generator  $Q$  can be shown to fulfill the relations [11]

$$\{Q, Q^\dagger\} = P^\mu, \quad (2.11)$$

$$\{Q, Q\} = \{Q^\dagger, Q^\dagger\} = 0, \quad (2.12)$$

$$[P^\mu, Q] = [P^\mu, Q^\dagger] = 0, \quad (2.13)$$

where  $P^\mu$  is the four momentum generator of spacetime translations. The squared mass operator  $-P^2$  commutes with  $Q$  and  $Q^\dagger$ , and all spacetime translation or rotation. It then follows that the supermultiplets has to have the same mass. However, if this was the case we should see plenty of supersymmetric partners everywhere, since most Standard Model particles have a mass well within detector range (the photon have, and thus its superpartner would have, mass  $m_\gamma = 0$ ). If we let Supersymmetry be a broken symmetry the Supersymmetric partners would have different mass and since no Supersymmetric particle have been found, Supersymmetry must be a broken symmetry.

The Minimal Supersymmetric Standard Model (MSSM) predicts a stable Lightest Supersymmetric Particle (LSP). If this particle is electrically neutral it can only interact weakly, making it a prime candidate as a WIMP. However, the stability of the LSP relies on R-parity  $P_R$  conservation. By construction R-parity assigns  $P_R = 1$  to Standard Model particles and  $P_R = -1$  to their superpartners and its conservation is introduced by hand in order to avoid catastrophic proton decay. Without a mechanism like R-parity conservation nothing prevents proton decay, for instance via  $p^+ \rightarrow e^+ \pi^0$  via a squark, since Supersymmetry violates baryon number conservation. We have yet to observe proton decay, so R-parity conservation satisfies observation but is not theoretically motivated.  $P_R$  conservation ensures that an LSP cannot decay further.

There is a possible candidate for the LSP in the neutralinos. Neutralinos are hypothetical fermions which are a mixture of the bino (superpartner of the  $U(1)$  gauge field corresponding to weak hypercharge), the neutral winos (superpartners to the W bosons of the  $SU(2)_L$  gauge fields) and the neutral higgsino (superpartner of the Higgs particle) yielding four different mass eigenstates [11]. The lightest neutralino is a massive stable particle and provides a possible candidate for cold dark matter. This particle could be produced thermally in the early universe, would couple to the weak force and the lightest neutralino would not be able to decay. However, it would be able to annihilate into Standard Model particles, some examples are presented in figure 2.7. When such a particle annihilate it would be able to observe passively through cosmic radiation as they decay into Standard Model particles.

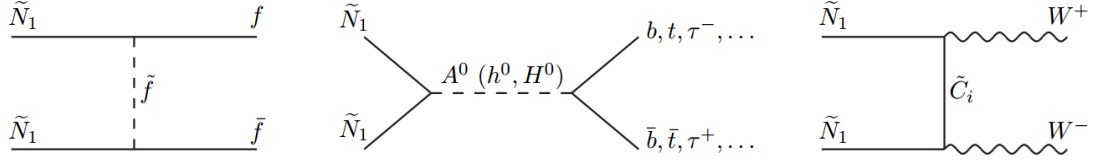


**Figure 2.7:** Some possible annihilation modes for the neutralino, from the left decay via slepton or squark, middle decay via Higgs and right via chargino.

### 2.3.3 Gravitino – decaying dark matter

By promoting Supersymmetry to a local theory we get a resulting theory called Supergravity. This theory necessarily unifies spacetime symmetries of ordinary general relativity with local Supersymmetry transformation [11]. The spin-2 graviton gains a spin-3/2 superpartner called gravitino. While the gravitino is initially massless, it gains mass by 'eating' the Goldstino in a manner similar to the Higgs mechanism in the Standard Model but by local symmetry breaking instead of electroweak symmetry breaking. Since its mass depends on the Supersymmetry breaking mechanism and could be any value.

Its interaction will be of gravitational strength and because of this it will be harder to detect than the WIMP and is instead classified as a superWIMP [12]. It will be almost impossible to detect it directly, and its annihilation cross section will be too small to produce enough cosmic rays to for it to be practical to detect. Additionally, if R-parity is not broken and the gravitino is the LSP there will be virtually no way of detecting it since it will not decay on its own. This combination may make it virtually impossible to detect dark matter. If R-parity is violated, however, the gravitino can decay, in which case it could be possible to detect it.

The gravitino Lagrangian  $\mathcal{L}_{3/2}$  is given by [13]

$$\mathcal{L}_{3/2} = -\frac{1}{2}\epsilon^{\mu\nu\rho\sigma}\bar{\psi}_\mu\gamma^5\gamma_\nu\partial_\rho\psi_\sigma - \frac{1}{4}m_{3/2}\bar{\psi}_\mu[\gamma^\mu, \gamma^\nu]\psi_\nu + \mathcal{L}_{int}. \quad (2.14)$$

Here  $\psi_\mu$  is the gravitino,  $m_{3/2}$  is the gravitino mass,  $\gamma^\nu$  are the Dirac matrices and  $\gamma^5 = i\gamma^0\gamma^1\gamma^2\gamma^3$ . The interaction part of the Lagrangian  $\mathcal{L}_{int}$  reads

$$\begin{aligned} \mathcal{L}_{int} = & -\frac{i}{\sqrt{2}M_{Pl}} \left[ (\tilde{\mathcal{D}}_\nu^*\phi^{*i})\bar{\psi}_\mu\gamma^\nu\gamma^\mu\chi_R^i - (\tilde{\mathcal{D}}_\nu\phi^i)\bar{\chi}_L^i\gamma^\mu\gamma^\nu\psi_\mu \right] \\ & -\frac{i}{8M_{Pl}}\bar{\psi}_\mu[\gamma^\nu, \gamma^\rho]\gamma^\mu\lambda^aF_{\nu\rho}^a + \mathcal{O}(M_{Pl}^{-2}) \end{aligned}, \quad (2.15)$$

where  $M_{Pl} = \frac{1}{\sqrt{G_N}}$  is the Planck scale and  $G_N$  the gravitational constant,  $\chi^i$  is the chiral fermion field,  $\phi^i$  is the scalar counterpart and the index  $i$  denote the species. The covariant derivative is given as

$$D_\nu\phi^i = (\partial_\mu\delta^{ij} + igT_{ij}^aA_\mu^a)\phi^j, \quad (2.16)$$

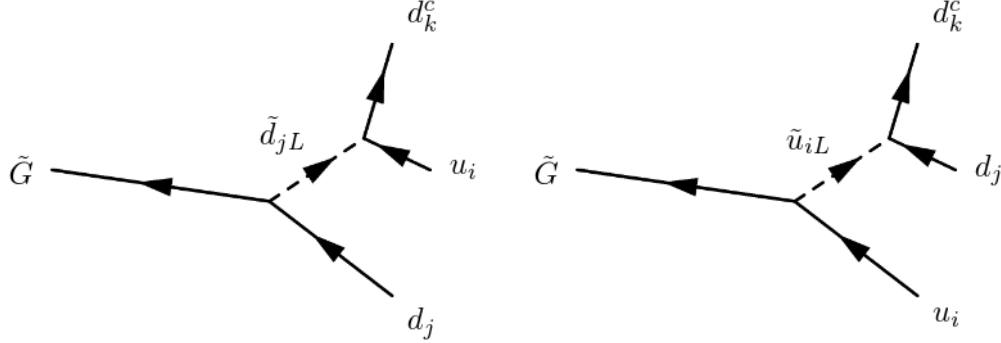


**Figure 2.8:** Gravitino decay into three antiquarks  $\tilde{G} \rightarrow \bar{q}\bar{q}\bar{q}$ . The arrows indicate the flow of momentum and the  $c$  superscript is charge conjugation indicating that all final state quarks are antiquarks. The gravitino connects to an antiquark and left handed squark as given in the interaction Lagrangian  $\mathcal{L}_{int}$ , while the squark can decay into two antiquarks as given in the R-parity violating part of the Lagrangian  $\mathcal{L}_{R_p}$ .

where  $F_{\mu\nu}^a$  are the field strength tensor for the gauge boson and  $T_{ij}^a$  with  $\alpha = 1, 2, 3$  are the generators of the Standard Model gauge groups. Finally, we also need the R-parity violating interactions  $\mathcal{L}_{R_p}$  where we have only included the term for the three generations of up  $u_i$  and down  $d_i$  quarks [14]

$$\mathcal{L}_{R_p} = \sum_{ijk} -\lambda''_{ijk} \frac{1}{2} \left( \tilde{u}_{iR}^* \bar{d}_{jR} d_{kL}^c + 2 \tilde{d}_{jR}^* \bar{u}_{iR} d_{kL}^c \right) + h.c., \quad (2.17)$$

where the  $c$  superscript is the charge conjugate, the  $*$  superscript is the complex conjugate, the  $R$  and  $L$  subscripts are the right and left chirality,  $\sim$  indicate the scalar superpartner and  $\lambda''_{ijk}$  is a dimensionless coupling constant. From this Lagrangian we can construct two Feynman diagrams with  $\tilde{G} \rightarrow \bar{q}\bar{q}\bar{q}$  as seen in figure 2.8. The gravitino initially decay to a antiquark and off-shelf squark. The off-shelf squark can then decay further via the R-parity violating coupling. The decay to three antiquarks are of special interest in cosmic ray antideuteron searches which will be discussed further in Chapter 3.



# Chapter 3

## Antideuteron searches

In this chapter I will discuss how to detect dark matter. I will make a case for why antideuterons are a good candidate for antimatter searches and discuss some experiments.

### 3.1 Antideuteron, a search channel with low noise

From Supersymmetry we have a few dark matter candidates. These candidates, while stable enough to account for dark matter, annihilate or decay into Standard Model particles depending on the model [15]. However, the universe is already populated with cosmic rays such as high energy protons. Dark matter signatures are expected to be very weak so we need to consider some search channel with a low background noise.

Figure 3.1 show some results from BESS-polar II showing a substantial proton and deuteron signal, as well as a solid antiproton signal. Conversely, antideuterons are very rare and thus could be a possible search channel for dark matter. Since dark matter candidates such as the neutralino can annihilate to Standard Model particles, they should produce a steady amount of antideuterons and be a source for a distinct antideuteron glow, making the antideuteron channel a promising channel for studying dark matter.

### 3.2 BESS-Polar II

The BESS-Polar II experiment flew over Antarctica in 2007-2008. BESS-Polar II investigated the origin of cosmic ray antiproton  $\bar{p}$ . While previous BESS experiments have identified most  $\bar{p}$  as secondary products of collisions between primary cosmic rays there were evidence primary  $\bar{p}$  were present. BESS-Polar II was an attempt to identify the source of remaining  $\bar{p}$ . Possible candidates for primary  $\bar{p}$  are primordial black holes evaporation and dark matter annihilation. The primordial black hole evaporation have a theoretical peak around 150 MeV, while

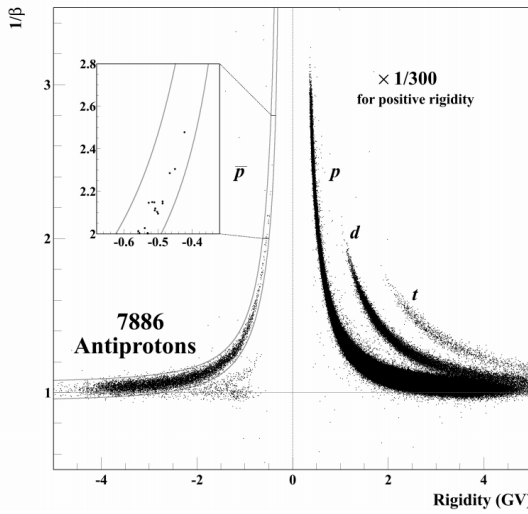


**Figure 3.1:** BESS-polar II detected antiprotons, but no deuterons. Only 1 in 300 positive rigidity events are shown, so very few  $e^+$  and  $\mu^+$  are seen. Lowest energy  $\bar{p}$ 's are shown in inset figure. Image is from [16].

secondary  $\bar{p}$  have a peak around 2 GeV. BESS-Polar II measure  $\bar{p}$  between 0.17 GeV and 3.5 GeV. The experiment could not detect any antideuterons as seen from figure 3.1.

### 3.3 AMS-02

The Alpha Magnetic Spectrometer (AMS-02) is particle physics experiment module mounted on the International Space Station (ISS) and is the only physics experiment on the space station. It is a detector designed to detect antimatter in cosmic rays. It uses a solenoid magnetic field to identify particles. It filters out any events which do not come from above to filter out contamination from the earth. The experiment as of 2015 has collected more than 60 billion cosmic ray events including electrons, positrons, protons, antiprotons and nuclei of helium, lithium, boron, carbon and oxygen. If antihelium is found it could be a sign that pockets of antimatter survive in space. Enough antihelium have been found that this needs to be investigated further.

AMS-02 have found that the antiproton to proton ratio stays constant at energies between 20 GeV and 450 GeV. This is contrary to what is expected from secondary antiprotons.

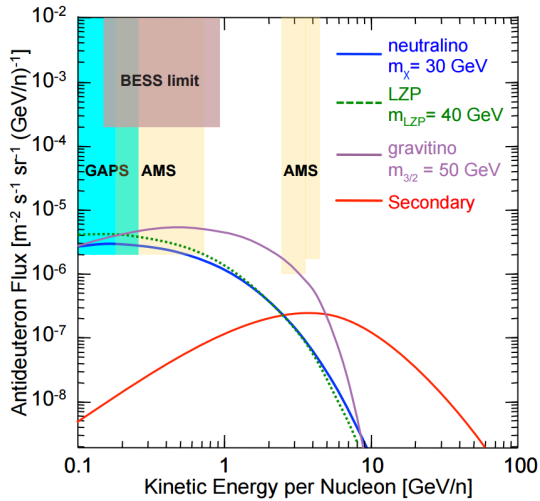


**Figure 3.2:** Detector sensitivity of BESS-polar II, AMS-02 and GAPS compared to predicted antideuteron flux at the top of the atmosphere. The solid blue line is antideuteron flux for the neutralino LSP with mass  $m_\chi \approx 30$  GeV, the solid purple line is for the gravitino LSP with mass  $m_{3/2} \approx 50$  GeV. The dashed green line is for right handed neutrinos with mass  $m_{LZP} \approx 40$  GeV. The solid red line is secondary deuterons produced in cosmic ray collisions. Image is from [10].

### 3.4 GAPS – the General AntiParticle Spectrometer

The GAPS experiment is specifically designed to detect antideuterons from cosmic rays. A GAPS science mission is proposed to fly over Antarctica in 2019-2020. The GAPS detection method relies on capturing antiparticles in a target material, producing exotic atoms. A time-of-flight system measures the direction and velocity of an incoming antiparticle. The antiparticle slows down and stops in the target material and forms an exotic atom in its excited state. When the exotic atom de-excites it emits X-rays. The X-rays uniquely determines the mass of the captured particle [10]. Finally, the antiparticle is captured by a nucleus of the target material and annihilates emitting annihilation products such as pions and protons. These annihilation products provide an additional means of identifying the parent antiparticle. The main background in the experiment are antiprotons since they also create exotic atoms. The X-ray signature and annihilation products should be sufficient to identify antideuterons from antiprotons. Additionally antideuterons will travel about twice as far in the target material given the same velocity compared to antiprotons which should give an excellent means of distinguishing antideuterons from antiprotons.



# Chapter 4

## Antideuteron production models

Here we will discuss two different models for creating antideuterons. The coalescence model is a model commonly used for deuteron production and is beginning to show some inaccuracies against new data from ALICE. A new model for antideuteron production, the cross section model, were recently proposed by Dal and Raklev [17].

### 4.1 Coalescence model

The Coalescence model is a simplified model used in Monte Carlo simulations describing the fusion of protons and neutrons into deuterons. It assumes that any proton and neutron caught within a sphere  $p_0$  in momentum space will fuse into a deuteron such that any pair with difference in momentum  $\Delta p < p_0$  in the center-of-mass-system will fuse.

Initially, in the coalescence model it was assumed isotropic and uncorrelated antiproton and antineutron spectra in order to obtain the analytical expression for antideuteron spectra in terms of the antiproton and antineutron spectra. Written with the adimensional variables  $x_i = T_i/M$ , where  $T_i$  is the kinetic energy for  $i \in \{\bar{p}, \bar{n}, \bar{d}\}$  and  $M$  is the dark matter particle mass, the spectrum is given by [18]

$$\frac{dN_d}{dx_d} = \frac{p_0^3}{3M^2m_p} \frac{1}{\sqrt{x_d^2 + 4m_p x_d/M}} \frac{dN_p}{dx_p} \frac{dN_n}{dx_n}, \quad (4.1)$$

where  $N_d$ ,  $N_p$  and  $N_n$  is the number of antideuterons, antiprotons and antineutrons respectively,  $p_0$  are the momentum threshold to create antideuteron and  $m_p \approx m_n \approx \frac{1}{2}m_d$  is the mass of the proton, neutron and deuteron respectively. This expression is suppressed by  $1/M^2$  for large dark matter mass  $M$ .

This expression must be wrong. For instance, considering the DM DM  $\rightarrow W^+W^-$  annihilation mode. A larger dark matter mass  $M$  will increase the boost of each  $W$ , but the number of antideuterons should stay constant as they are produced from  $W$  decay. This back to back jet production is common enough

that for any dark matter particle considerably heavier than the proton the expected spectrum would be wrong. This flaw in the model can be traced back to the assumption of spherical symmetry in proton and neutron production [18]. Because of this we will have to obtain and apply  $p_0$  on a per event basis when used for a Monte Carlo simulation.

The threshold value  $p_0$  is a phenomenological value and experiments show that this value changes depending on the experiment, yielding a range of values depending on the process producing the nucleons and the energy involved. Some contributing factors are the hadronization models which leads to different predictions not apparent in a primary spectrum, but may become apparent with secondary spectra created with the coalescence model [19]. Additionally, in collider simulations the  $p_0$  value seem to shift depending on the collider energy. This poses a problem with regards to expected spectra whenever the process happens outside of a particle accelerator.

The coalescence model can be expressed as a step function dependent on the difference between the nucleon momenta  $k$  being less than some threshold value  $p_0$

$$P(\bar{p}\bar{n} \rightarrow \bar{d}|k) = \theta(p_0 - k). \quad (4.2)$$

That the coalescence model is defined by a step function is reason to think the model ought to be flawed considering the Standard Model is based on QFT. We would therefore expect some continuous probability distribution for the formation of deuterons instead. This will be discussed further in chapter 4.2.

The Monte Carlo simulator we use is PYTHIA 8 and we use  $p_0 = 0.2$  TeV value from [20]. As mentioned earlier we apply the coalescence model on a per event basis to account for non-isotropic formation of jets during particle collisions. Additionally, we do not account for spin correlation in the center-of-mass system and the influence it has on the angular distributions and may be a source for error, but we suspect it is small since in the lab frame such an effect should be small due to the large boost [17].

In the model we check each event, where an event is when two protons collide, for at least one proton and one neutron which also are a finalstate particle. If there are at least one of each finalstate nucleons we attempt to create a deuteron. If successful we combine their 3-momentum to create  $\mathbf{p}_d = \mathbf{p}_p + \mathbf{p}_n$  and find the energy by  $E_d = \sqrt{p_d^2 + m_d^2}$ . When doing this we accept a violation of conservation of energy  $\Delta E = E_d - (E_p + E_n)$  which we assume is radiated away by a photon at some later stage, but this is not modeled.

We also do not consider distance between the final state particles. Since weakly interacting particles have macroscopic decay lengths while deuteron formation typically happens on the femtometer scale, distance between candidates should be considered as the nucleons need to be close enough together to create a deuteron. However, very few antideuterons are expected to be created by decaying finalstates [17] and we will not consider distance between candidates in our

simulations since deuteron creation should rarely be suppressed due to distance for this reason.

## 4.2 Cross section model

The Coalescence model assumes a sharp threshold to form antideutrons where a deuteron always forms for a difference in momentum less than the threshold. This type of model can not capture effects of specific processes such as resonances which may happen at different energies and it is natural to assume that the coalescence model can not be applied universally and needs recalibration depending on the energy range of the experiment.

To account for this Raklev and Dal have developed an alternative model for anti deuteron formation [19]. In this model the probability of deuteron formation depends on the cross section for antideuteron formation for each combination of  $\bar{p}$  and  $\bar{n}$

$$P(N_i N_j \rightarrow \bar{d}X | k) = \frac{\sigma_{N_i N_j \rightarrow \bar{d}X}(k)}{\sigma_0}, \quad (4.3)$$

where  $\sigma_{N_i N_j \rightarrow \bar{d}X}$  is a sum of processes with an antideuteron in the final state,  $k$  is the difference in momentum given in equation 4.2 and  $\{N_i, N_j\} \in \{\bar{p}, \bar{n}\}$  is the different combinations of nucleons which can fuse to make  $\bar{d}$ . The probability is normalised to a reference cross section  $\sigma_0$ , which is a free parameter, like  $p_0$  in the coalescence model, and needs to be experimentally fitted to the data. The processes which were considered are listed in table 4.1

- |   |   |
|---|---|
| 1) $\bar{p}\bar{n} \rightarrow \bar{d}\gamma$     | 5) $\bar{p}\bar{p} \rightarrow \bar{d}\pi^-$      |
| 2) $\bar{p}\bar{n} \rightarrow \bar{d}\pi^0$      | 6) $\bar{p}\bar{p} \rightarrow \bar{d}\pi^-\pi^0$ |
| 3) $\bar{p}\bar{n} \rightarrow \bar{d}\pi^+\pi^-$ | 7) $\bar{n}\bar{n} \rightarrow \bar{d}\pi^+$      |
| 4) $\bar{p}\bar{n} \rightarrow \bar{d}\pi^0\pi^0$ | 8) $\bar{n}\bar{n} \rightarrow \bar{d}\pi^+\pi^0$ |

**Table 4.1:** Processes considered in the cross section model

For each of these processes a fit to published data were used to find an approximate cross section. For the  $\bar{p}\bar{n} \rightarrow \bar{d}\gamma$  photoproduction process the function to be fitted was

$$\frac{\sigma_{\bar{n}\bar{p} \rightarrow \bar{d}\gamma}(\kappa)}{1 \mu\text{b}} = \begin{cases} \sum_{n=-1}^{10} a_n \kappa^n & : \kappa < 1.28 \\ \exp(-b_1 \kappa - b_2 \kappa^2) & : \kappa \geq 1.28, \end{cases} \quad (4.4)$$

where  $\kappa = k/(1 \text{ GeV})$  and the parameters are given in table 4.2. Above  $\kappa = 1.28$  an exponential form was chosen to avoid the function diverging or obtaining negative numbers at high energies.

Parameter	Value
$a_{-1}$	2.30346
$a_0$	$-9.366346 \times 10^1$
$a_1$	$2.565390 \times 10^3$
$a_2$	$-2.5594101 \times 10^4$
$a_3$	$1.43513109 \times 10^5$
$a_4$	$-5.0357289 \times 10^5$
$a_5$	$1.14924802 \times 10^6$
$a_6$	$-1.72368391 \times 10^6$
$a_7$	$1.67934876 \times 10^6$
$a_8$	$-1.01988855 \times 10^6$
$a_9$	$3.4984035 \times 10^5$
$a_{10}$	$-5.1662760 \times 10^4$
$b_1$	-5.1885
$b_2$	2.9196

**Table 4.2:** Best fit values to the parameters given in equation 4.4

For the  $N_i N_j \rightarrow \bar{d}\pi$  processes isospin invariance was used to obtain the relations

$$\sigma_{pn \rightarrow d\pi^0} = \frac{1}{2} \sigma_{pp \rightarrow d\pi^+}, \quad (4.5)$$

and

$$\sigma_{nn \rightarrow d\pi^-} = \sigma_{pp \rightarrow d\pi^+}. \quad (4.6)$$

For the process  $pp \rightarrow d\pi^+$  Machner [21] have previously made a best fit

$$\sigma(\eta) = \frac{a\eta^b}{(c - \exp(d\eta))^2 + e}, \quad (4.7)$$

with parameters given in table 4.3. Here  $\eta = q/m_{\pi^+}$  and  $q$  is the momentum of the pion in the COM frame. Machner only found a fit for the  $pp \rightarrow d\pi^+$  process and the rest was assumed to be similar enough to use the same cross section. This relation is not exact, since the isospin symmetry is broken due to the differing nucleon and pion masses. The processes  $nn \rightarrow d\pi^-$  and  $pp \rightarrow d\pi^+$  use the best fit for  $pn \rightarrow d\pi^0$  due to the isospin relations.

For the  $ij \rightarrow \bar{d}\pi\bar{\pi}$  processes isospin predicts the relations

$$\sigma_{pn \rightarrow d\pi^+\pi^-} = 2\sigma_{pn \rightarrow d\pi^0\pi^0} + \frac{1}{2}\sigma_{pp \rightarrow d\pi^+\pi^0}, \quad (4.8)$$

and

$$\sigma_{nn \rightarrow d\pi^-\pi^0} = \sigma_{pp \rightarrow d\pi^+\pi^0}. \quad (4.9)$$

Parameter	Value
$a [\mu b]$	0.17
$b$	1.34
$c$	1.77
$d$	0.38
$e$	0.096

**Table 4.3:** Best fit values for equation 4.7

Parameter	Value
$a [\mu b]$	$2.855 \times 10^6$
$b$	$1.311 \times 10^1$
$c$	$2.961 \times 10^3$
$d$	$5.572 \times 10^0$
$e$	$1.461 \times 10^6$

**Table 4.4:** Best fit values for the  $pn \rightarrow d\pi^0\pi^0$  process.

Parameter	Value
$a_1 [\mu b]$	$6.465 \times 10^6$
$b_1$	$1.051 \times 10^1$
$c_1$	$1.979 \times 10^3$
$d_1$	$5.363 \times 10^0$
$e_1$	$6.045 \times 10^5$
$a_2 [\mu b]$	$2.549 \times 10^{15}$
$b_2$	$1.657 \times 10^1$
$c_2$	$2.330 \times 10^7$
$d_2$	$1.119 \times 10^1$
$e_2$	$2.868 \times 10^{16}$

**Table 4.5:** Best fit values for the  $pn \rightarrow d\pi^+\pi^-$  process.

Parameter	Value
$a [\mu b]$	$5.099 \times 10^{15}$
$b$	$1.656 \times 10^1$
$c$	$2.333 \times 10^7$
$d$	$1.133 \times 10^1$
$e$	$2.868 \times 10^{16}$

**Table 4.6:** Best fit values for the  $pp \rightarrow d\pi^+\pi^0$  process.

Based on the similarities with equation 4.7 the functional forms used for the fits were

$$\sigma(\kappa) = \frac{a\kappa^b}{(c - \exp(d\kappa))^2 + e}, \quad (4.10)$$

for  $pp \rightarrow d\pi^+\pi^0$  and  $pn \rightarrow d\pi^0\pi^0$ , and

$$\sigma(\kappa) = \frac{a_1\kappa^{b_1}}{(c_1 - \exp(d_1\kappa))^2 + e_1} + \frac{a_2\kappa^{b_2}}{(c_2 - \exp(d_2\kappa))^2 + e_2}, \quad (4.11)$$

for  $pn \rightarrow d\pi^+\pi^-$ .

### 4.2.1 Finalstate kinematics

For the coalescence model we need to find the magnitude of the difference in momentum  $k = |\mathbf{p}_p - \mathbf{p}_n|$ . In the center-of-mass System the total momentum is defined to be  $\mathbf{p}_{tot} = \mathbf{p}_p + \mathbf{p}_n = 0 \implies \mathbf{p}_p = -\mathbf{p}_n = \mathbf{p}$  which yields

$$|\mathbf{p}_p - \mathbf{p}_n| = |2\mathbf{p}| = 2p = k \quad (4.12)$$

where  $p$  is the momentum absolute value of either the proton and neutron in the center-of-mass system. In order to boost from the Lab system to the center-of-mass system we will Lorentz boost with the requirement that the total momentum in the center-of-mass reference frame needs to be  $\mathbf{p}_{tot} = \mathbf{0}$ .

In **Pythia 8** [22] the particle properties are by default given in the Lab reference frame. Since the momentum absolute value  $p$  is given in the center-of-mass frame we have to first boost the particle to the center-of-mass frame to apply the model to check for deuteron production, and later back to the Lab frame to compare it to what a detector would see. Using natural units, the Lorentz transformations are

$$\begin{bmatrix} E \\ \mathbf{0} \end{bmatrix} = \Lambda' \begin{bmatrix} E' \\ \mathbf{p}' \end{bmatrix}, \quad (4.13)$$

when boosting from the Lab system to the center-of-mass frame, and

$$\begin{bmatrix} E' \\ \mathbf{p}' \end{bmatrix} = \Lambda \begin{bmatrix} E \\ \mathbf{0} \end{bmatrix}, \quad (4.14)$$

when boosting from the center-of-mass back to the Lab system.  $E$  is energy and  $\Lambda$  is the Lorentz boost matrix. The boost is connected to the reverse boost by  $\Lambda'(\beta) = \Lambda(-\beta)$ . The Lab system is primed, while center-of-mass system is unprimed.

Now lets consider two particles 1 and 2. The squared four-momentum  $p^2 = s$  is invariant:

$$E^2 = (E'_1 + E'_2)^2 - (\mathbf{p}_1' + \mathbf{p}_2')^2 = s \quad (4.15)$$

where  $s$  is one of the invariant Mandelstam variables.

The total center-of-mass energy is  $E = E_1 + E_2 = \sqrt{p^2 + m_1^2} + \sqrt{p^2 + m_2^2}$  and we can use this to solve for the center-of-mass momentum magnitude  $p$  directly while only depending on the mandelstam variable  $s$  which allows us to avoid the explicit use of Lorentz boosting.

$$p = \frac{[(s - (m_1 + m_2)^2)(s - (m_1 - m_2)^2)]^{1/2}}{2\sqrt{s}} \quad (4.16)$$

The momentum absolute value  $p$  is the momentum of either particles 1 or 2 in the center-of-mass frame.

When finding the difference in momentum  $k$  for any processes we use the mass of the incoming particles and obtain  $k$  from the relation  $k = 2p$  from equation (4.12).

When considering two-particle finalstates, to find the absolute value of the deuteron momentum in the center-of-mass frame we can use equation (4.16) and insert the mass of the deuteron and the mass of the second particle. For instance in the process  $\bar{p}\bar{n} \rightarrow \bar{d}\pi^0$  we get the deuteron absolute momentum  $p_{\bar{d}}$  by exchanging  $m_1 \rightarrow m_{\bar{d}}$  and  $m_2 \rightarrow m_{\pi^0}$ .

For three-particle decays finding the momentum of the deuteron is more complex. We refer to the section on three-particle decays in Particle Data Group Collaboration [23]. We define the combined four-momentum of two particles as  $p_{ij} = p_i + p_j$  and the combined mass as  $m_{ij}^2 = p_{ij}^2$ . We define the total 4-momentum  $P$  in the center-of-mass system as

$$P = p_1 + p_2 + p_3 = (\sqrt{s}, \mathbf{0}), \quad (4.17)$$

such that the invariant Mandelstam variable  $s$  is

$$P^2 = s, \quad (4.18)$$

leading to

$$(P - p_3)^2 = s + m_3^2 - 2\sqrt{s}E_3, \quad (4.19)$$

but also

$$(P - p_3)^2 = (p_1 + p_2)^2 = m_{12}^2. \quad (4.20)$$

Combining equations (4.19) and (4.20) we can solve for  $|\mathbf{p}_3|^2$  which gives

$$|\mathbf{p}_3| = \sqrt{\left(\frac{s + m_3^2 - m_{12}^2}{2\sqrt{s}}\right)^2 - m_3^2}, \quad (4.21)$$

or equation (46.20b) in ParticleDataGroup [23],

$$|\mathbf{p}_3| = \frac{[(s - (m_{12} + m_3)^2)(s - (m_{12} - m_3)^2)]^{1/2}}{2\sqrt{s}}. \quad (4.22)$$

Here, the momentum  $|\mathbf{p}_3|$  is given in the center-of-mass frame.

Assigning for example  $1 \rightarrow \pi, 2 \rightarrow \pi, 3 \rightarrow d$  yields

$$|\mathbf{p}_d| = \frac{[(s - (m_{\pi\pi} + m_d)^2)(s - (m_{\pi\pi} - m_d)^2)]^{1/2}}{2\sqrt{s}}. \quad (4.23)$$

To find the mass  $m_{12}$  we refer to the Dalitz plot [23]. The upper bound for the mass  $m_{12}$  in the Dalitz plot is  $(m_{12}^2)_{max} = (\sqrt{s} - m_3)^2$ . The lower bound is  $(m_{12}^2)_{min} = (m_1 + m_2)^2$ . In the Dalitz plot it is assumed isotropic decay. To determine the final 4-momentum for particle 3 the mass  $m_{12}$  is first determined:

$$m_{12} = [x((m_{12})_{max}^2 - (m_{12})_{min}^2) + (m_{12})_{min}^2]^{1/2} \quad (4.24)$$

where  $x \in \{0, 1\}$  is a uniformly distributed random number.

Once the deuteron absolute value momenta is known we will choose a direction for it by assuming the deuteron is formed isotropically. We pick a number between the angles  $\phi \in (0, 2\pi)$  and  $\theta \in (0, \pi)$  in spherical coordinates giving us the 4-momenta in the center-of-mass frame. If we choose the angles uniformly in the given range we get a higher probability to pick a direction near the poles ( $\theta$  near 0 and  $\pi$ ). To prevent this we will choose the direction by choosing  $z$  and  $\theta$  in the ranges

$$z \in \{1, -1\}, \theta \in \{2\pi, 0\}, \quad (4.25)$$

and from this choose the  $x$  and  $y$  coordinates as

$$x = \sqrt{1 - z^2} \cos \theta \quad (4.26)$$

$$y = \sqrt{1 - z^2} \sin \theta, \quad (4.27)$$

finally finding the deuteron 4-momentum by

$$\begin{bmatrix} E_d \\ (p_d)_x \\ (p_d)_y \\ (p_d)_z \end{bmatrix} = \begin{bmatrix} \sqrt{p_d^2 + m_d^2} \\ xp_d \\ yp_d \\ zp_d \end{bmatrix}, \quad (4.28)$$

in the CMS frame.

We then need to boost the deuteron from CMS back to the lab frame using the Lorentz matrix  $\Lambda(-\beta)$

$$\Lambda(-\beta) = \begin{bmatrix} \gamma & \gamma\beta n_x & \gamma\beta n_y & \gamma\beta n_z \\ \gamma\beta n_x & 1 + (\gamma - 1)n_x^2 & (\gamma - 1)n_x n_y & (\gamma - 1)n_x n_z \\ \gamma\beta n_y & (\gamma - 1)n_x n_y & 1 + (\gamma - 1)n_y^2 & (\gamma - 1)n_y n_z \\ \gamma\beta n_z & (\gamma - 1)n_x n_z & (\gamma - 1)n_y n_z & 1 + (\gamma - 1)n_z^2 \end{bmatrix}. \quad (4.29)$$

Here the unit vector  $\mathbf{n}$  is the spatial direction of the boost.

If we study the initial particles  $N_i N_j$  we can find the proper Lorentz boost to go back to the original Lab frame.

$$\begin{bmatrix} E'_{N_i} + E'_{N_j} \\ \mathbf{p}'_{N_i} + \mathbf{p}'_{N_j} \end{bmatrix} = \Lambda(-\beta) \begin{bmatrix} E_{N_i} + E_{N_j} \\ 0 \end{bmatrix} = (E_{N_i} + E_{N_j}) \gamma \begin{bmatrix} 1 \\ \beta n_x \\ \beta n_y \\ \beta n_z \end{bmatrix}. \quad (4.30)$$

Here  $E_{N_i} = \sqrt{p_{N_i}^2 + m_{N_i}^2}$  is the energy in the center-of-mass reference frame for nucleon  $k$ . From this we construct the  $\Lambda$  matrix and use this to boost the deuteron back to the lab frame with the variables

$$\gamma = \frac{E'_{N_i} + E'_{N_j}}{E_{N_i} + E_{N_j}}, \quad (4.31)$$

$$\beta = \sqrt{1 - \frac{1}{\gamma^2}}, \quad (4.32)$$

and

$$\mathbf{n} = -\frac{1}{\beta \gamma (E_{N_i} + E_{N_j})} (\mathbf{p}'_{N_i} + \mathbf{p}'_{N_j}). \quad (4.33)$$

We now have the particle kinematics required for deuteron formation with the models previously discussed.

### 4.3 Comparing models to experiment

With the models outlined above I will try and replicate Dal's results [17]. Deuteron and antideuteron spectra in  $p\bar{p}$  minimum bias events at 0.9, 2.76 and 7 TeV have been measured by the ALICE experiment at the LHC [20]. In addition to minimum bias, ALICE also uses a trigger (V0AND) which suppresses single diffractive events by requiring activity on opposite sides of the interaction point. To simulate this trigger we turn off diffractive events, and let **Pythia 8** only produce non diffractive events. This still produces a small error and we compensate by weighting the spectrum with  $f_{ND,trig} = 0.861$ . This value is the average value taken for 7 TeV found by Dal taken from his table IX [17]. We did not try and tune this value since its contribution was small compared to other contributions when implementing the models and used this value for all experiments. For the simulation we used **Pythia 8.186**.

In figure (4.1) we compare our results for antideuterons compared to Lars results and ALICE for 7 TeV, 2.76 TeV and 0.9 TeV. We used  $p_0 = 0.2$  GeV from [20] in all energy regimes and we used the values for  $\sigma_0$  taken from [17] and are shown in table 5.1. It is immediately apparent that our implementation

Experiment	Coalescence	Cross section
7 TeV	1.10	1.34
2.76 TeV	1.15	1.39
0.9 TeV	1.15	1.44

**Table 4.7:** Average factor difference between the results in this thesis compared to L. Dal's results [17]

produce too many antideuterons. When studying the Coalescence results from figure 4.1 it appears our results are overshooting by a fixed factor across the spectrum and is true for the 7 TeV, 2.76 TeV and 0.9 TeV spectrums. The factors are listed in table 4.7. Since we used  $p_0 = 0.2$  GeV for all coalescence plots, this could be improved using the  $p_0$  values from [17], but we ran out of time for this thesis.

The cross section model has a different slope between Lars implementation and the implementation done here and does not only differ by a fixed factor. While we used the variables and fits found at [17], we seem to catch more deuterons at lower transverse momentum  $p_T$ . We used a different  $f_{ND,trig}$  factor at 2.76 TeV and 0.9 TeV energies, but this fails to explain the difference. This difference in slope gives a particularly bad fit for the cross section model in our case and we can only assume we failed to implement the model properly.

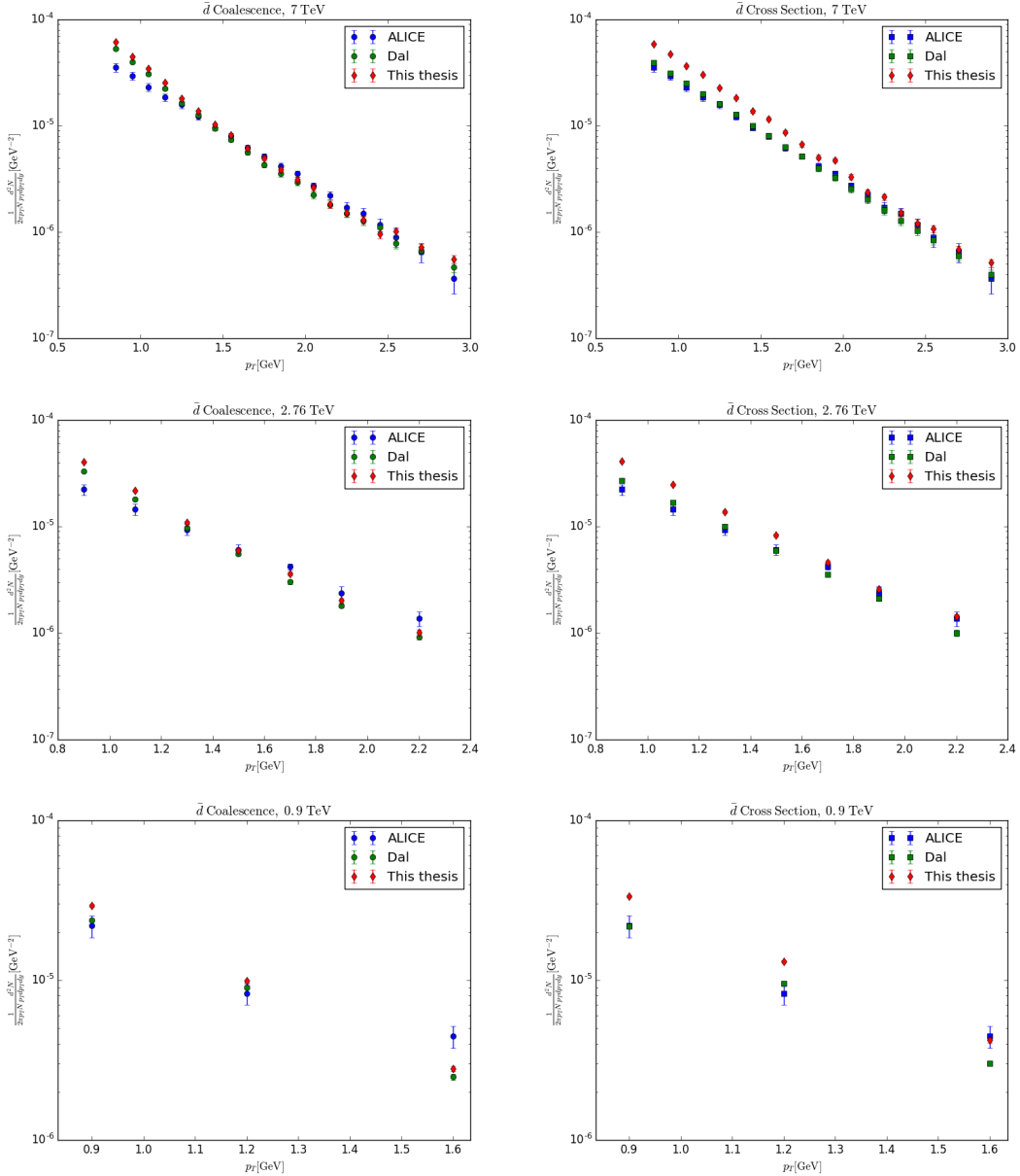


**Figure 4.1:** Comparison between this thesis, results from [17] and results from ALICE [20]. Rapidity is  $|y| < 0.5$ . Top is 7 TeV, middle 2.76 TeV and bottom 0.9 TeV. On the left is the Coalescence model and on the right is the Cross section model.



# Chapter 5

## Improving antideuteron production models

In this chapter we will discuss how to improve the antideuteron models described in chapter 4 by first studying the proton spectrum. If the models used by **Pythia 8** provide a proton spectrum that differ from experiment, we will assign weights to adjust the spectrum to better fit experiment and use these weights when producing deuterons. We will see if the spectrum of the coalescence and the cross section models are improved.

### 5.1 Comparing measured $p$ and $\bar{p}$ spectra to Monte Carlo models

There are some errors in Monte Carlo models, partly due to limitations due to modelling, for instance the hadronization model decide how many baryons we get from quarks and gluons. The deuteron production models are limited by how good the prediction of the input  $\bar{p}$  and  $\bar{n}$  spectra are. From figure 5.1 we see that there are some discrepancies between experiment and the spectrum by Pythia. Particularly for low transverse momentum Pythia 8 have a tendency to overshoot the results from experiment. These differences should lead to some error in the deuteron models as well and improving the proton spectrum should lead to better deuteron spectrums as well. From figure 5.2 we see that the predicted neutron spectrum is almost identical to the proton spectrum and because of this will we use the proton spectrum from ALICE to assign weights to the neutron spectrum as well.

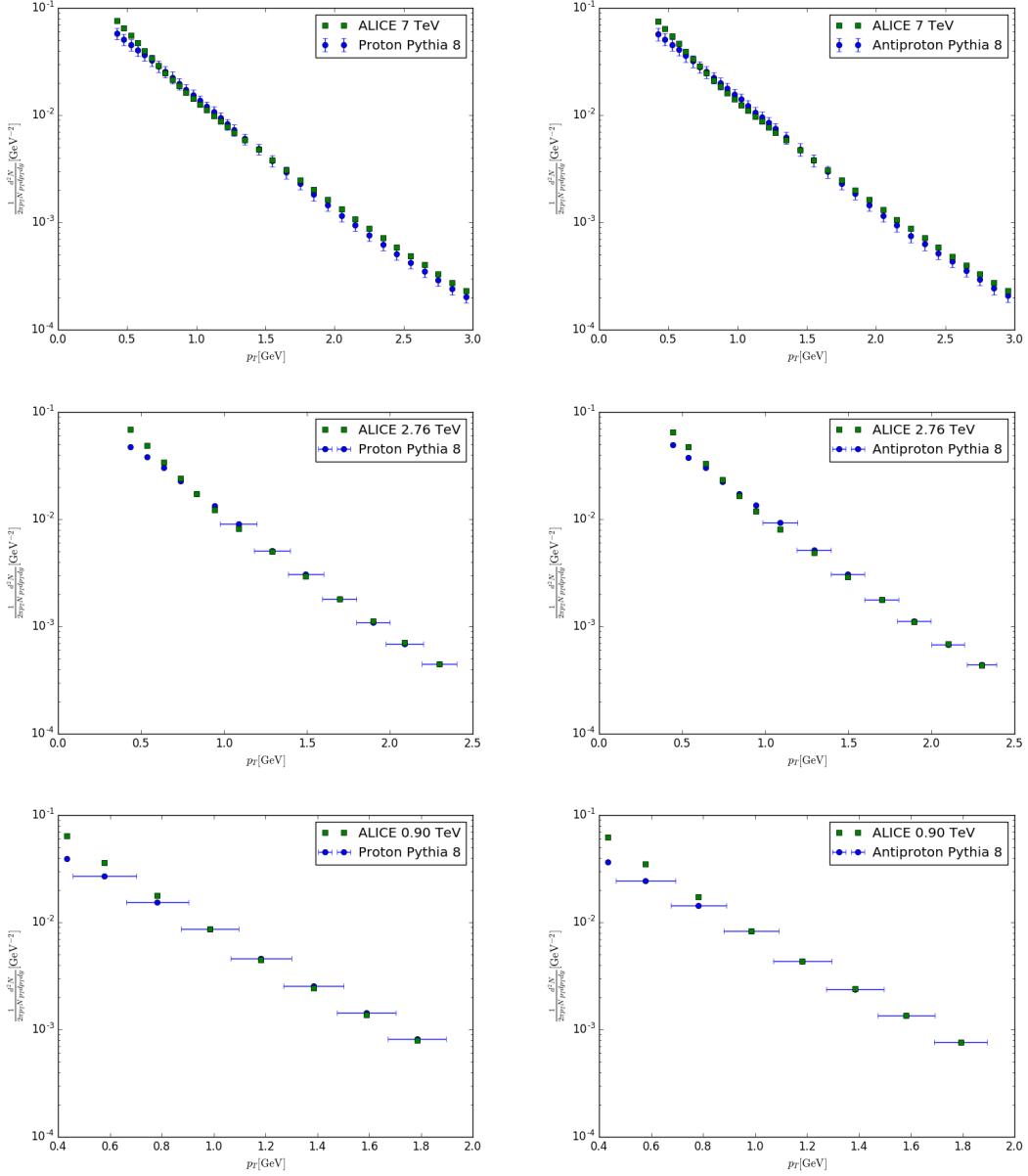


**Figure 5.1:** Minimum bias proton spectra measured by the ALICE experiment. The ALICE data shown here is taken from a preliminary analysis [20]. Top  $\sqrt{s} = 7 \text{ TeV}$ , middle  $\sqrt{s} = 2.76 \text{ TeV}$  and bottom  $\sqrt{s} = 0.9 \text{ TeV}$ , rapidity  $|y| < 0.5$ . On the left is the proton spectrum and on the right is the antiproton spectrum produced by Pythia 8.

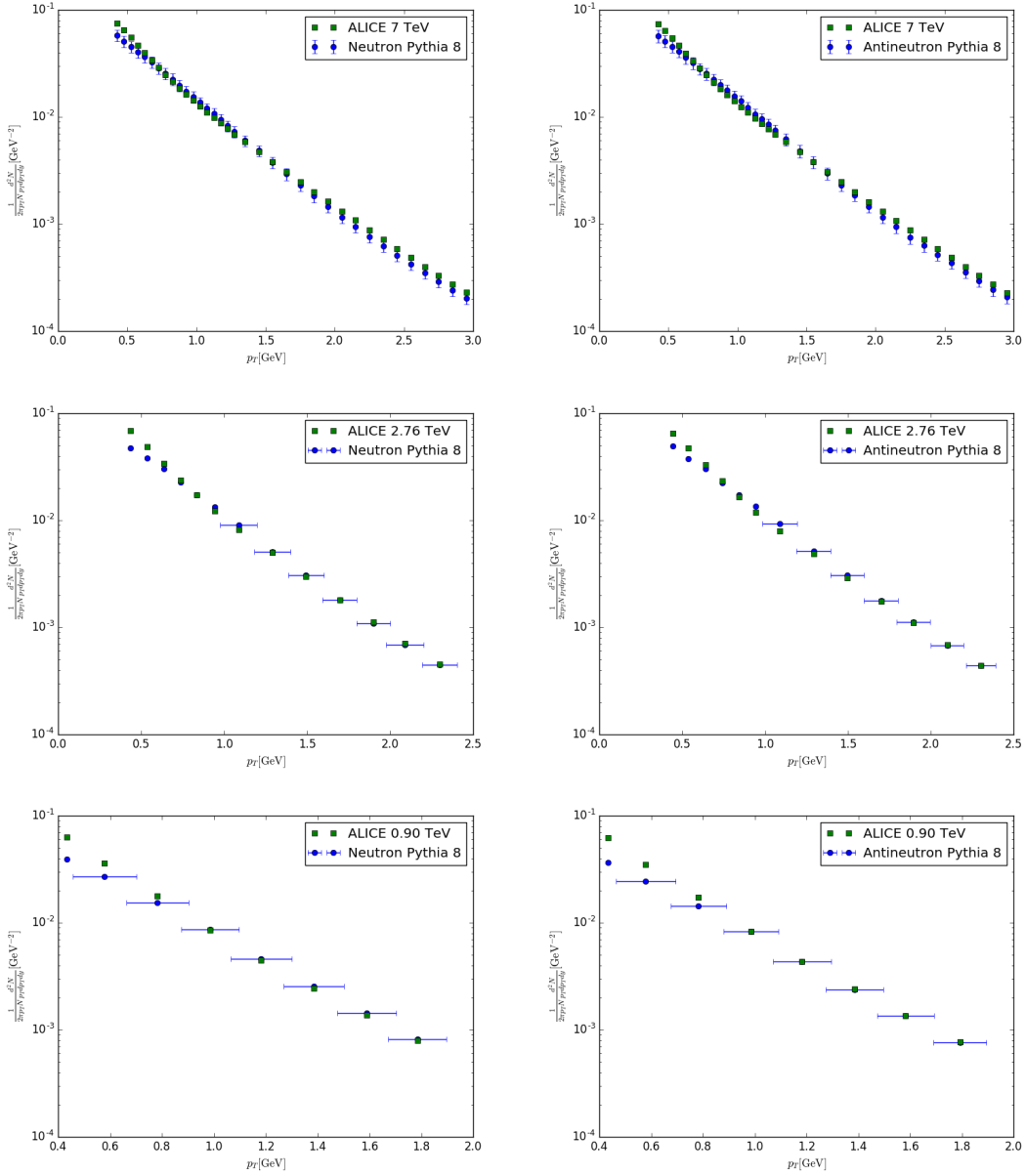


**Figure 5.2:** Minimum bias proton spectra measured by the ALICE experiment. The ALICE data shown here is taken from a preliminary analysis [20]. Top  $\sqrt{s} = 7 \text{ TeV}$ , middle  $\sqrt{s} = 2.76 \text{ TeV}$  and bottom  $\sqrt{s} = 0.9 \text{ TeV}$ , rapidity  $|y| < 0.5$ . On the left is the neutron spectrum and on the right is the antineutron spectrum produced by Pythia 8.

## 5.2 Reweighting

As described in 5.1, there are some differences in the proton and antiproton spectra produced by the Monte Carlo simulator and the results from ALICE. These differences can lead to errors in the deuteron spectrum. To improve the initial proton spectrum we can assign weights to the protons so the Monte Carlo spectrum fits better with experiment. We can adjust the Monte Carlo results by assigning them weights according to

$$w_i = \frac{p_i^{exp}}{p_i^{MC}} \quad (5.1)$$

where  $p_i^{exp}$  is the number of protons from experiment in bin  $i$ ,  $p_i^{MC}$  is the number of protons in bin  $i$  from Monte Carlo simulation and  $w_i$  is the weight assigned to the  $i$ 'th bin. We also need to reweight neutrons. However, since neutrons are neutral particles we do not have a spectrum from experiment. They should have a very similar spectrum to the protons at such high energies and we use the proton spectrum to reweight Monte Carlo neutrons as well in the same manner we do protons.

When deuterons are produced the weights of the parent particles are multiplied  $w_j^d = w_j^{N_1} w_j^{N_2}$  and assigned to the  $j$ 'th deuteron. In this manner the deuteron spectrum should be suppressed or enhanced in roughly the same region of momentum space as the parent particles.

Some shortcomings in this method is that we only know the spectra as a function of momentum and in a restricted region in rapidity  $y$ , since the experiment does not have sensors in the beam path. The rapidity is restricted to  $|y| = 0.5$  [20]. We do not know the angular correlation between  $\bar{p}$  and  $\bar{n}$ . Also, the weights outside the measured proton spectrum will also contribute to the deuteron spectrum and we choose to assign a weight of 1 per particle for these particles. Because of this we expect to see tapering towards the unweighted deuteron spectrum near the endbins.

## 5.3 Reweighted $\bar{d}$ spectra

The reweighted spectrums are shown in figure 5.3 and figure 5.4. The spectrums are minimal bias with the requirement rapidity  $|y| < 0.5$ .

From figure 5.4 and 5.3 the reweighting method had more effect on the coalescence model compared to the cross section model. We suspect the reason for this is that the coalescence model draw parents with similar momentum while the cross section model takes weight samples more spread out in momentum space. Another notable effect is that the endpoints of the experimental data, especially in the coalescence model, seems to snap back towards an unweighted spectrum. To avoid this we suggest extrapolating the weight distribution some distance out

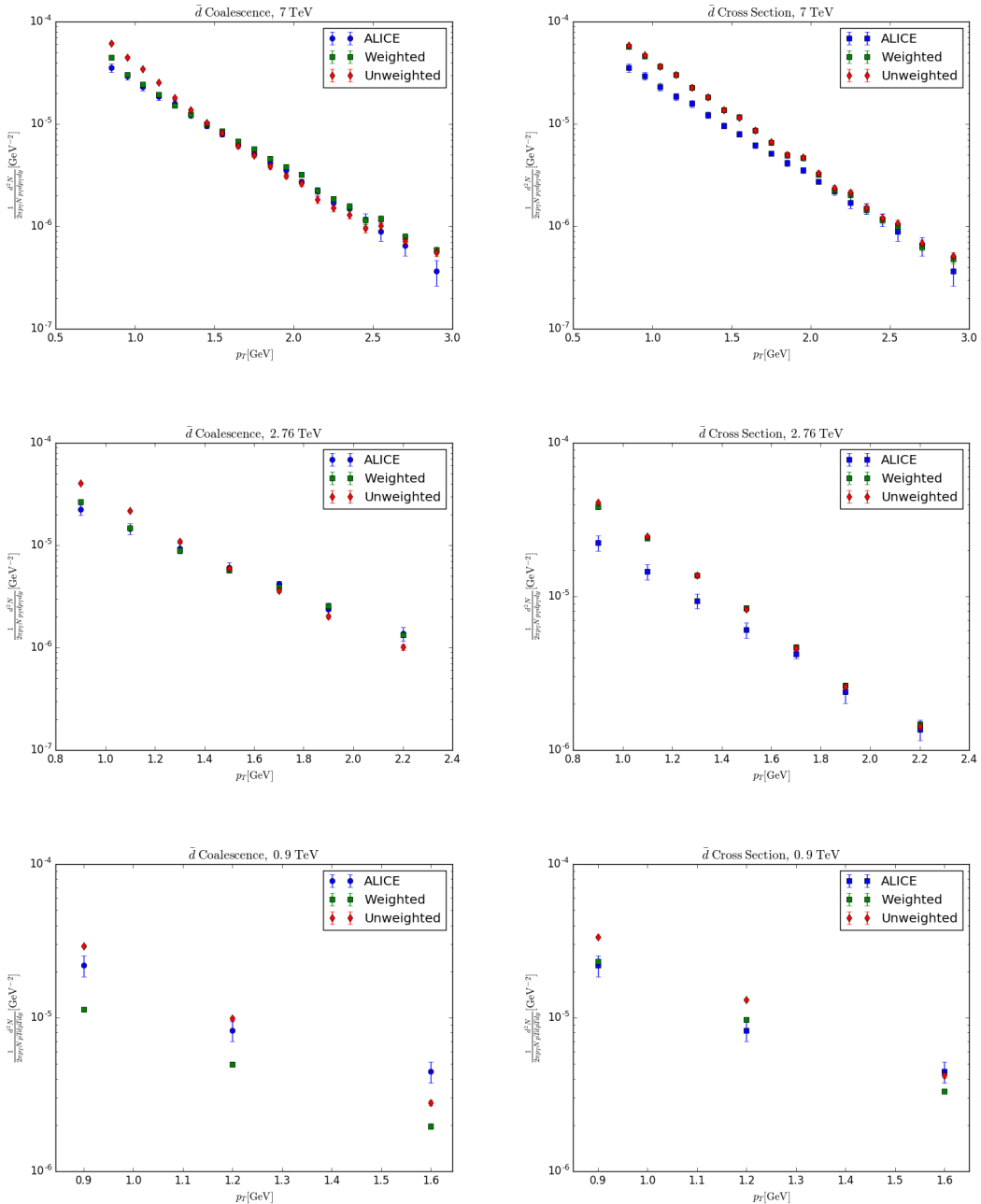


**Figure 5.3:** Antideuteron comparison. Top 7Tev, middle 2.76TeV and bottom 0.9TeV. Left: Coalescence model, right: Cross section model.

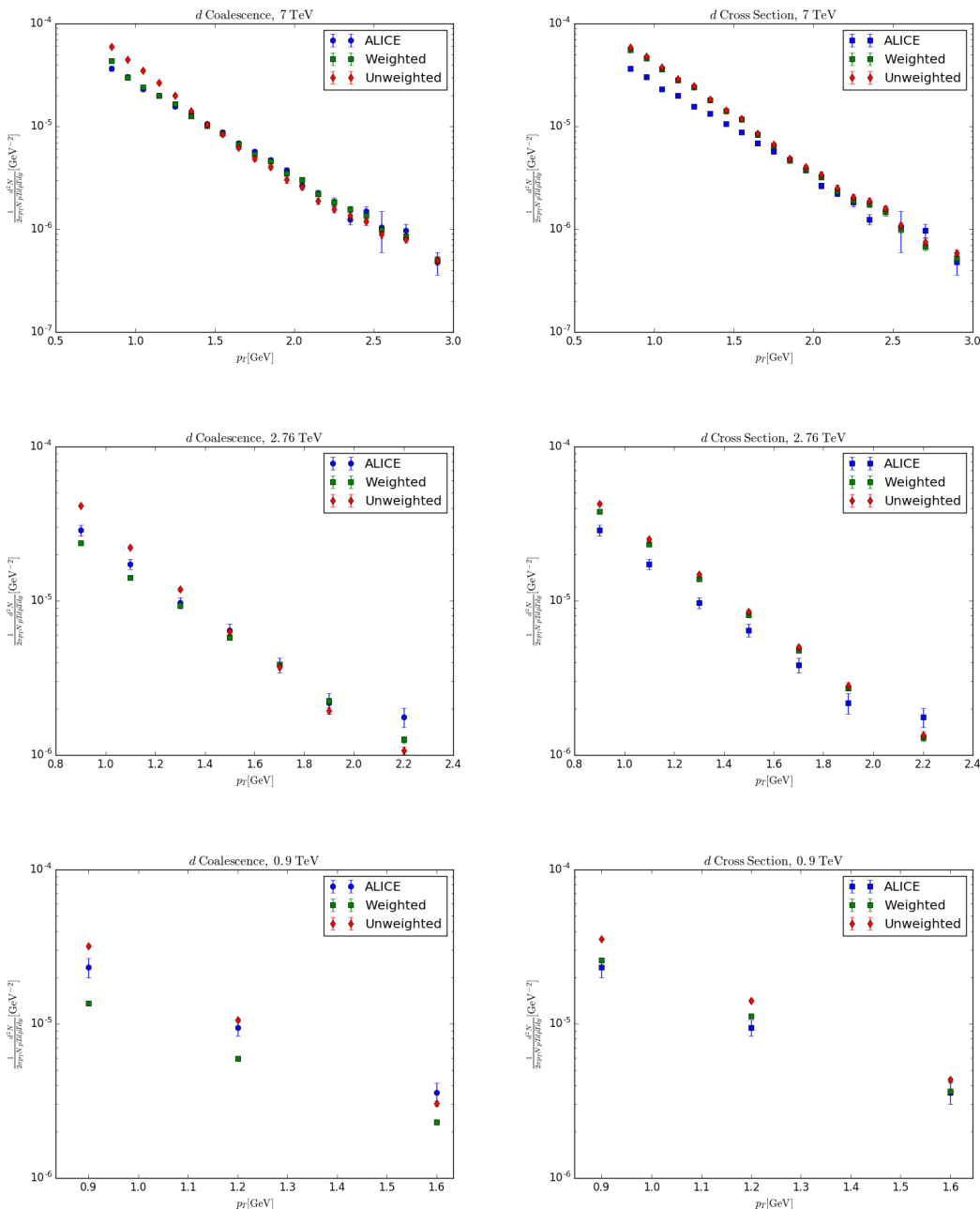


**Figure 5.4:** Deuteron comparison. Top 7Tev, middle 2.76TeV and bottom 0.9TeV. Left: Coalescence model, right: Cross section model.

Experiment	$p_0$ [GeV]	$\chi^2_{p_0}$	$\chi^2_{p_0}$ weight	$\frac{1}{\sigma_0}$ [barn $^{-1}$ ]	$\chi^2_{\sigma_0}$	$\chi^2_{\sigma_0}$ weight
$d$ , 7 TeV	0.2	469	32.4	2.63	945	756
$\bar{d}$ , 7 TeV	0.2	178	40.5	2.58	504	474
$d$ , 2.76 TeV	0.2	53.9	14.9	2.88	128	77.9
$\bar{d}$ , 2.76 TeV	0.2	79.4	4.77	2.93	117	104
$d$ , 0.9 TeV	0.2	8.42	22.6	3.58	30.9	2.92
$\bar{d}$ , 0.9 TeV	0.2	12.0	29.1	3.63	27.0	4.31

**Table 5.1:** Caption

from the experimental data to avoid deuterons sampling near the edge of the experimental proton spectrum.

The spectrum resulting from the cross section appears to have been assigned a small weight and it is not obvious the weighting method had much effect on the spectrum. In figure 5.5 we have listed the average weight  $|w_i|$  in the different bins  $i$  of the spectrums. As noted earlier, the coalescence model has a small snap back effect near the edges of the spectrum, while the cross section model does not have an obvious such effect. Additionally the coalescence weight distribution is fluctuating more.

To investigate this further we tracked which parent particles fused to produce deuterons. In figure 5.6 the momentum of the different parent particles are tracked. We only count combinations which creates a deuteron, and one parent is counted according to its transverse momentum along the x-axis and the other parent along the y-axis. In the coalescence model protons are always on the x-axis, while neutrons are always on the y-axis. For the cross section model the parent nucleons can be two protons or neutrons (see table 4.1), so we have both protons and neutrons on both axis. The different methods produce distinct distributions in momentum space. The coalescence model tends to sample the parents close together in momentum. The cross section model by contrast has a much wider selection range.

This may help to explain the weight distributions in figure 5.5 and why the cross section model yields averaged weights compared to the coalescence model. We speculate that the weighting method for the cross section model is more useful for a wider spectrum, but has the unintended side effect of smoothing out the spectrum with the danger of erasing details.

To compare the different tests, we use  $\chi^2$  test.

$$\chi^2 = \sum_{i=0}^n \frac{(d_i - m_i)^2}{\sigma_i^2} \quad (5.2)$$

where  $d_i$  is the data from experiment,  $m_i$  is what the model predicts and  $\sigma_i$  is the experimental error, all at the datapoint  $i$ . From table 5.1 we have overall better fits for the weighted methods, and the cross section method benefitted

the most. The cross section method generally have very poor fits and because of this it is hard to know whether the results here are valid. We see from figure 5.5 that the cross section method are adjusted according to the proton spectrum, so if the original fit were better we can speculate that the cross section method gains a greater relative benefit. On the other hand, considering the steep slope difference between our implementation and the original it is hard to know if the wide sample size from 5.6 is an artefact due to poor implementation.

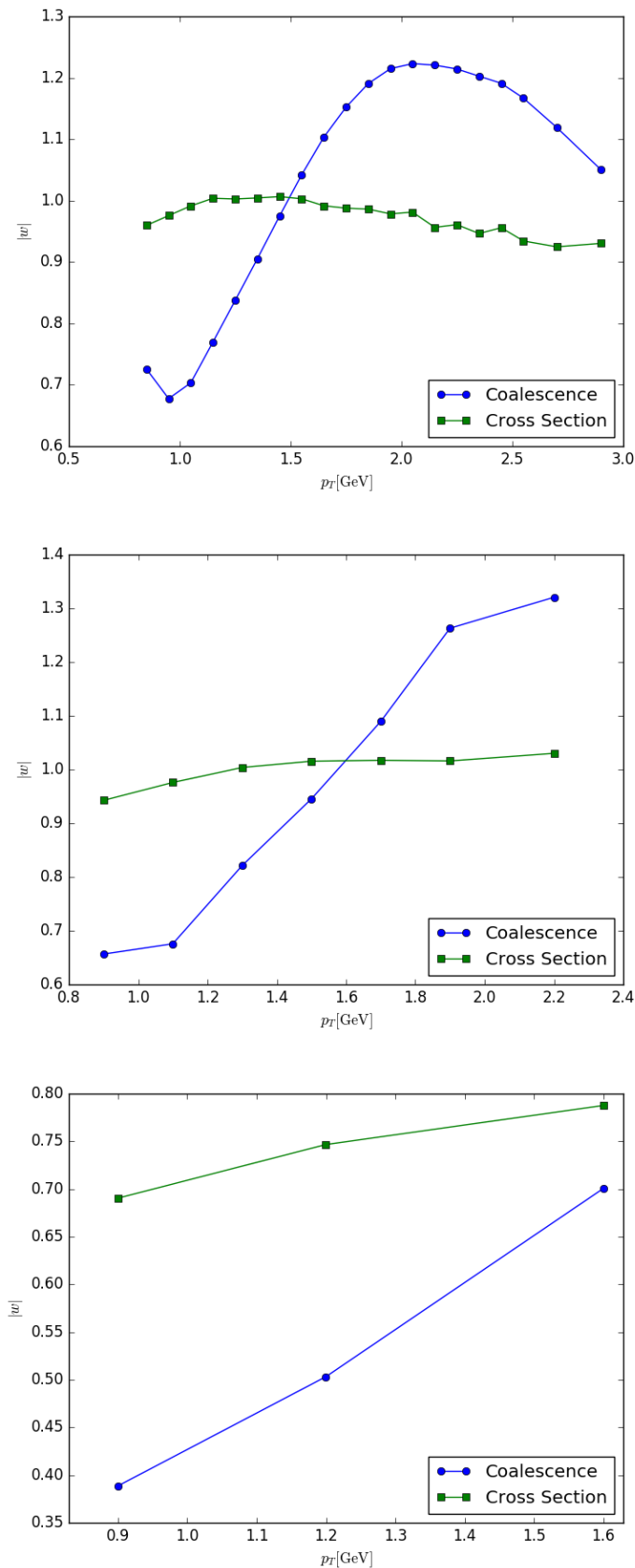


**Figure 5.5:** Comparison of weights between Coalescence and Cross section models.

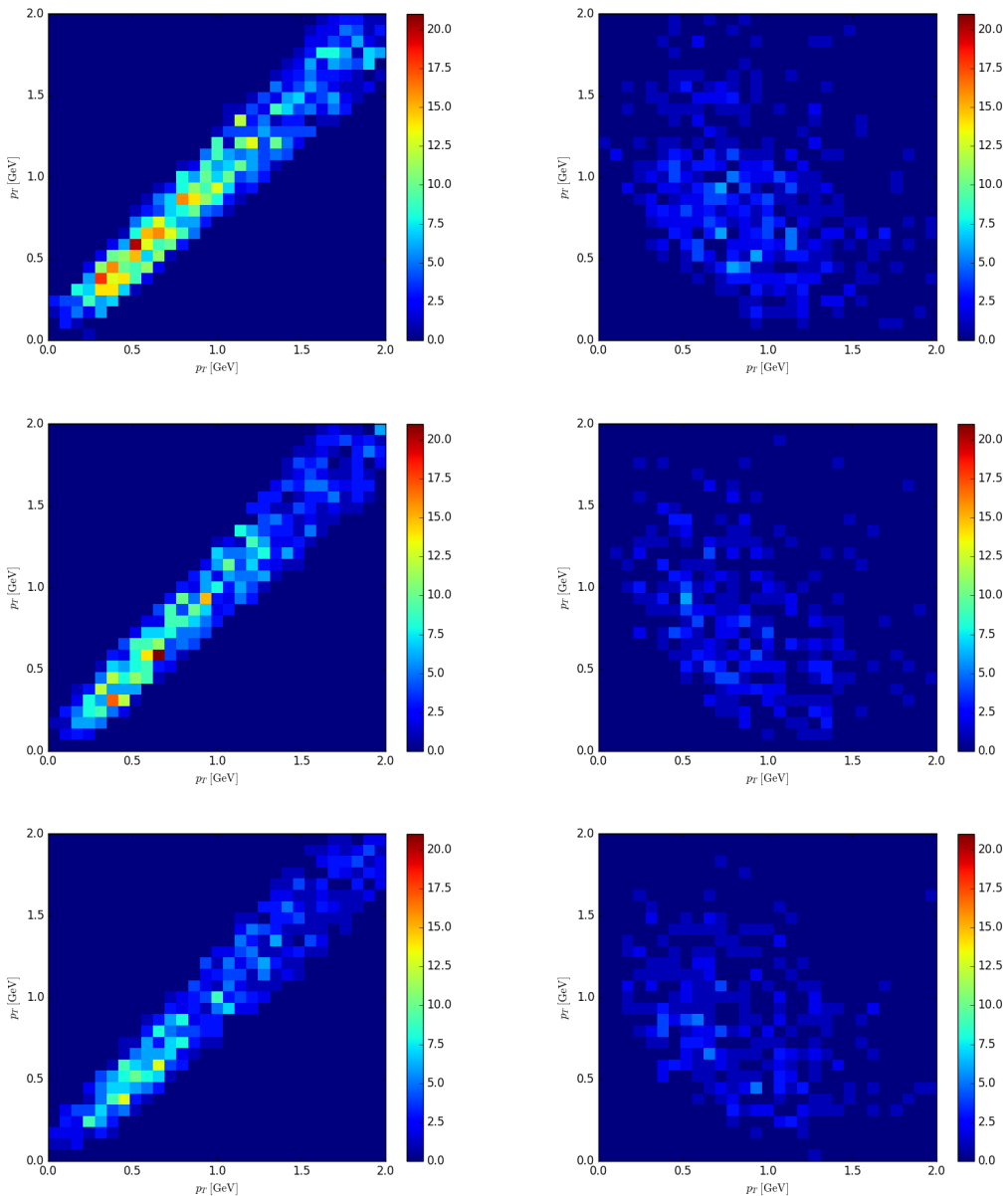


**Figure 5.6:** Map of the transverse momentum of the particles used to combine to deuterons. The x-axis is  $p_T$  of particle 1, and y-axis is  $p_T$  of particle 2. Top: 7TeV, middle: 2.76TeV, bottom: 0.9TeV. Left: Coalescence, Right: Cross section.

# Chapter 6

## Conclusion

In this thesis we have attempted to implement two different methods for deuteron formation for Monte Carlo simulators. The two models are the coalescence model and the cross section model. The coalescence model has a very different physical interpretation than the cross section model, as the cross section model is designed more like a field theory taking account of resonances for nucleon capture, while the coalescence model are more classical in that it guarantees nucleon capture for low enough momentum difference.

The cross section model also takes more processes into account so such as  $\bar{p}\bar{p} \rightarrow \bar{d}X$ , while the coalescence model is limited to  $\bar{p}\bar{n} \rightarrow \bar{d}X$ . Both models, however, depend on one variable which needs to be fitted to data. Still, our implementation of the coalescence model proved more successful than the cross section model.

We also have tried a weighting method to improve two different deuteron production methods for Monte Carlo simulators. We found that the coalescence method appear to work well with the weighting method, but the cross section method have picks weights over a very wide momentum range limiting the improvement. However, since our implementation of the cross section method seems to be flawed it is hard to know how limited the weighting method are when applied to a well fitted spectrum by the cross section method.



# Bibliography

- [1] F. Zwicky, *On the Masses of Nebulae and of Clusters of Nebulae*, *Astrophys. J.* **86** (1937) 217–246.
- [2] V. C. Rubin and W. K. Ford, Jr., *Rotation of the Andromeda Nebula from a Spectroscopic Survey of Emission Regions*, *Astrophys. J.* **159** (1970) 379–403.
- [3] Ø. Grøn, *Einstein’s General Theory of Relativity*. Springer, 2007.
- [4] P. Natarajan *et. al.*, *Mapping substructure in the HST Frontier Fields cluster lenses and in cosmological simulations*, *Mon. Not. Roy. Astron. Soc.* **468** (2017) 1962–1980, [[arXiv:1702.04348](#)].
- [5] WMAP: C. L. Bennett *et. al.*, *Nine-Year Wilkinson Microwave Anisotropy Probe (WMAP) Observations: Final Maps and Results*, *Astrophys. J. Suppl.* **208** (2013) 20, [[arXiv:1212.5225](#)].
- [6] S. Y. Hoh, J. Komaragiri, and W. A. T. B. W. Abdullah, *Dark Matter Searches at the Large Hadron Collider*, *AIP Conf. Proc.* **1704** (2016) 020005, [[arXiv:1512.07376](#)].
- [7] T. Marrodñ Undagoitia and L. Rauch, *Dark matter direct-detection experiments*, *J. Phys.* **G43** (2016) 013001, [[arXiv:1509.08767](#)].
- [8] S. Funk, *Indirect Detection of Dark Matter with gamma rays*, [arXiv:1310.2695](#). [Proc. Nat. Acad. Sci.112,2264(2015)].
- [9] L. Baudis, *Direct dark matter detection: the next decade*, *Phys. Dark Univ.* **1** (2012) 94–108, [[arXiv:1211.7222](#)].
- [10] T. Aramaki *et. al.*, *Review of the theoretical and experimental status of dark matter identification with cosmic-ray antideuterons*, *Phys. Rept.* **618** (2016) 1–37, [[arXiv:1505.07785](#)].
- [11] S. P. Martin, *A Supersymmetry primer*, [hep-ph/9709356](#). [Adv. Ser. Direct. High Energy Phys.18,1(1998)].

- [12] L. A. Dal, *Cosmic Ray Antideuterons from Particle Dark Matter*. PhD thesis, University of Oslo, 2015.
- [13] M. Grefe, *Unstable Gravitino Dark Matter - Prospects for Indirect and Direct Detection*. PhD thesis, Hamburg U., 2011. [arXiv:1111.6779](https://arxiv.org/abs/1111.6779).
- [14] G. Moreau and M. Chemtob, *R-parity violation and the cosmological gravitino problem*, *Phys. Rev.* **D65** (2002) 024033, [[hep-ph/0107286](https://arxiv.org/abs/hep-ph/0107286)].
- [15] F. Donato, N. Fornengo, and P. Salati, *Anti-deuterons as a signature of supersymmetric dark matter*, *Phys. Rev.* **D62** (2000) 043003, [[hep-ph/9904481](https://arxiv.org/abs/hep-ph/9904481)].
- [16] K. Abe *et. al.*, *Measurement of the cosmic-ray antiproton spectrum at solar minimum with a long-duration balloon flight over Antarctica*, *Phys. Rev. Lett.* **108** (2012) 051102, [[arXiv:1107.6000](https://arxiv.org/abs/1107.6000)].
- [17] L. A. Dal and A. R. Raklev, *Alternative formation model for antideuterons from dark matter*, *Phys. Rev.* **D91** (2015) 123536, [[arXiv:1504.07242](https://arxiv.org/abs/1504.07242)]. [Erratum: Phys. Rev.D92,no.8,089901(2015)].
- [18] M. Kadastik, M. Raidal, and A. Strumia, *Enhanced anti-deuteron Dark Matter signal and the implications of PAMELA*, *Phys. Lett.* **B683** (2010) 248–254, [[arXiv:0908.1578](https://arxiv.org/abs/0908.1578)].
- [19] L. A. Dal and M. Kachelriess, *Antideuterons from dark matter annihilations and hadronization model dependence*, *Phys. Rev.* **D86** (2012) 103536, [[arXiv:1207.4560](https://arxiv.org/abs/1207.4560)].
- [20] E. Serradilla, *Producin de nclos de deutero y antideutero en el experimento ALICE del LHC*. PhD thesis, Madrid, CIEMAT, 2013.
- [21] H. Machner and J. Niskanen, *Charge independence studied in  $NN \rightarrow d\pi$  reactions*, *Nucl. Phys.* **A776** (2006) 172–188, [[nucl-ex/0511027](https://arxiv.org/abs/nucl-ex/0511027)].
- [22] T. Sjostrand, S. Mrenna, and P. Z. Skands, *A Brief Introduction to PYTHIA 8.1*, *Comput. Phys. Commun.* **178** (2008) 852–867, [[arXiv:0710.3820](https://arxiv.org/abs/0710.3820)].
- [23] Particle Data Group: K. A. Olive *et. al.*, *Review of Particle Physics*, *Chin. Phys.* **C38** (2014) 090001.